Copyright

by

Scott Allan Eckley

2018

The Thesis Committee for Scott Allan Eckley
Certifies that this is the approved version of the following Thesis:

3D Textural and Geochemical Analyses on Carbonado Diamond: Insights from Pores and the Minerals Within Them

APPROVED BY
SUPERVISING COMMITTEE:

Richard A. Ketcham, Supervisor

John C. Lassiter

Nathaniel R. Miller

3D Textural and Geochemical Analyses on Carbonado Diamond: Insights from Pores and the Minerals Within Them

by

Scott Allan Eckley

Thesis

Presented to the Faculty of the Graduate School of

The University of Texas at Austin

in Partial Fulfillment

of the Requirements

for the Degree of

Master of Science in Geological Sciences

The University of Texas at Austin

May, 2018

Dedication

To Larry Taylor, my late undergraduate advisor, for pushing me to become a better scientist, introducing me to diamond geology, and putting me in contact with my current advisor.

Acknowledgements

I would like to thank many people for their help and encouragement along the way. First and foremost, my advisor Dr. Richard Ketcham has been an invaluable source of insight, direction, and motivation. In addition to being a phenomenal scientist who is enthusiastic about his work and others', he is also a genuinely caring advisor.

Dr. Miller has provided crucial expertise and advice for all things dealing with ICP-MS. His attention to detail and unending patience were necessary as I stumbled through the actual analyses and data reduction.

Dr. Lassiter's knowledge of mantle geochemistry was useful for interpreting data that have basically never been acquired or interpreted before.

This project would not have been possible without the entire UTCT staff and lab group. Having no background in XCT, I felt like I was thrown into the deep end without knowing how to swim. However, Jessie Maisano, Matt Colbert, Dave Edey, Romy Hanna, Gary Zuker, and Kylie Wright were amazing resources and quickly made me feel welcomed. They provided motivation, technical support, advice, and endless snacks.

Ed Marshall and Staci Loewy were incredibly helpful during sample preparation for geochemical analyses. The Stockli lab group helped with age-dating zircons.

To my wonderful friends that I made during graduate school: you are sincere, fun, and intelligent. There is never a dull moment with you all. I will never forget the weekends of tubing down the Colorado River, evenings of volleyball, nights of shenanigans, camping trips, parties, and evening beers at Crown.

Everything I have been able to do in my life so far is because of the upbringing my family gave me. Thank you Mom, Dad, Nicole, Brett, Roger, and Azur. I wish I could visit more, but know that I love you and miss you all every day.

As I am writing this, I cannot help from thinking about previous teachers and professors. Thank you to my most influential high school teachers, Mr. Verble, Ms. Mathews, Mrs. Allen, and Mr. McDowd, for preparing me for the world and sparking creativity and curiosity. To Dr. Gray, Dr. McSween, and Dr. Taylor, you transformed my interests in the Earth into a passion for geology.

Finally, the past two years would have been very different without the most loving and kind girlfriend. Kelly, you have become my best friend and most trusting confidant.

Abstract

3D Textural and Geochemical Analyses on Carbonado Diamond: Insights from Pores and the Minerals Within Them

Scott Allan Eckley, M.S. Geo. Sci.

The University of Texas at Austin, 2018

Supervisor: Richard A. Ketcham

Carbonado is an enigmatic variety of polycrystalline diamond found only in placer deposits in Brazil and the Central African Republic, with unknown primary origin. These highly porous dark nodules possess a narrow range of isotopically light carbon ($\delta^{13}C$ -31 to -24 ‰), a primarily crustal inclusion suite unusually enriched in REEs and actinides filling the pore spaces, a loosely constrained crystallization age between 2.6 and 3.8 Ga, and other atypical features which have led to a variety of formation theories, from extra-solar to deep mantle. Unravelling the circumstances responsible for the diamond material and inclusion suite may provide evidence of not-yet-understood mantle processes and/or geochemical reservoirs.

This study represents the first multi-sample 3D textural analysis of carbonado diamond using high resolution X-ray computed tomography. We document a variety of textures in both pore structure and mineralogy within pores. All samples feature a foliation with a mild preferred orientation. We observe the same fabric in a framesite diamond, a less porous polycrystalline diamond found in kimberlites and thought to crystallize shortly

before eruption. The similarity in fabrics suggests a similar process could have formed both. Additionally, spatially coherent 3-D volumes of pores with similarly attenuating filling material juxtaposed against volumes with differently attenuating material suggests that secondary minerals formed from the spatially-limited *in-situ* breakdown of primary inclusion phases. These observations, combined with the presence of euhedral cavities and pseudomorphs, supports the hypothesis that the material comprising the secondary minerals within carbonado is largely primary.

Step-leaching and ICP analysis of three African and two Brazilian samples reveals that the modern-day inclusion suite is highly enriched in REE (average ΣREE = 2.3 wt. %), with REE and trace element patterns that match those of melts derived from low degree (< 1 %) partial melting of primitive mantle (*i.e.* kimberlite and carbonatite), suggesting a link between carbonado and primitive melts.

These textural and chemical findings support the origin of both carbonado and its pore-filling material in a mantle environment. The origin of light carbon in the mantle before 2.6 Ga remains unknown, but subduction of organic material is a possible mechanism.

Table of Contents

List of Tables

List of Figures

Chapter 1: Introduction to Carbonado Diamonds

1.1 MOTIVATION

Diamonds are unevenly distributed trace minerals in the crust, but aside from some large impact craters and ultra-high-pressure metamorphic terranes, almost all are formed in the mantle at depths of ~150 to 800 km. Crystallizing from mobile carbon-bearing fluids/melts, they are entrained as xenocrysts in volatile-rich, rapidly-ascending volcanic host rocks (i.e. kimberlites, lamproites, and lamprohyres) (Shirey et al., 2013). Because of their incredible strength and chemical inertness they are able to preserve mineral and fluid inclusions that were incorporated during diamond growth. The chemical and physical nature of these inclusions may thus provide clues to the origin of diamonds at depths greater than 150 km. Furthermore, because diamonds have been forming since 3.5 Ga, inclusion analysis may help understand the origin and nature of carbon in the mantle through time (Shirey and Richardson, 2011).

This thesis endeavors to identify the genetic environment of an unusual type of diamond, carbonado. Carbonado is an enigmatic variety of polycrystalline diamond thought to have formed in the Archean and found only in alluvial placer deposits in the Central African Republic and Brazil (Trueb and Butterman, 1969; Trueb and De Wys, 1969, 1971). These dark nodules are irregularly shaped and typically range from millimeter to centimeter size, with the “Carbonado of Sergio” being the largest diamond ever found, weighing 3,167 carats (Haggerty, 1999). Other varieties of polycrystalline diamond (*i.e.* framesite, ballas, bort, and stewardite) are commonly found in kimberlites. They are distinguished from carbonado by being less porous or completely pore-free, hosting large amounts of syn-genetic silicate inclusions and/or magnetic minerals, contrasting external morphology (spherical) (Haggerty, 2014). They are thought to have rapidly crystallized

from carbon-bearing fluids shortly before or during kimberlite emplacement. Because most kimberlite magmatism is Neoproterozoic or younger (Stern and Miller, 2018), non-carbonado polycrystalline diamonds document relatively young diamond-forming events. From the aforementioned differences, carbonado is primarily distinguished from other varieties of polycrystalline diamond by hosting an extensive network of pores with sizes from < 1 μm to > 1 mm that comprise ~ 15 % of their volume. These pores are filled with an assemblage of minerals that evidently equilibrated at crust P-T conditions.

Several diverse theories have been proposed to explain carbonado diamond origins, including meteorite impact (Kamioka et al., 1996; Smith and Dawson, 1985), irradiation of crustal carbon (Ozima et al., 1991), extra-terrestrial (Garai et al., 2006; Haggerty, 2014), and formation within a unique mantle environment (Ishibashi et al., 2012; Kagi and Fukura, 2008; Ketcham and Koeberl, 2013), with no consensus reached over the 50 years they have been studied. In addition to its industrial use as a particularly tough abrasive, the diversity of proposed origins, with potential to elucidate new processes and geochemical reservoirs, makes resolving the mystery of carbonado formation a scientifically intriguing topic. Establishing a mantle origin would allow carbonado to be used to make interpretations about various aspects of the Archean mantle: (a) the origin of isotopically light carbon in the mantle at > 2.6 Ga; (b) the link between diamond formation and incompatible-element-rich fluids/melts thought to play a major role in metasomatism; (c) and redox heterogeneities.

To further understand how carbonado formed, we focus on the pore network and the material within it. Little research has investigated the internal textures of carbonado or characterized the chemical compositions of the pore-filling material. This study provides the first multi-sample examination of internal textures and incompatible-element data on the material within carbonado's pore network. We use these data to expand upon recent

models hypothesizing that carbonado formed in a fluid-rich environment within the mantle (Ishibashi et al., 2012; Kagi and Fukura, 2008; Ketcham and Koeberl, 2013; Petrovsky et al., 2010).

1.2 CARBONADO BACKGROUND

The origin of carbonado has eluded consensus for multiple reasons. Their tough physical nature hinders typical preparation techniques, restricting *in situ* analyses to small pieces that have been laboriously polished, fractured, or laser cut. From the relatively few studies that have successfully prepared and analyzed carbonado, an extensive list of physical and chemical characteristics have been observed or measured that are challenging to reconcile with known diamond-forming environments. The following background information outlines these characteristics and revises previous hypotheses posed for their formation.

1.2.1 Geologic Setting

Carbonado was originally mined from placer deposits in Brazil starting in the mid-19th century and a reported ~2 metric tons have been recovered from both Brazil and the Central African Republic (Haggerty, 2014). Compared to the ~600 metric tons of diamond that have been mined from kimberlites since the 1870s, carbonado represents a small fraction of total diamond production (Haggerty, 2014) Their absence from typical diamondiferous rocks (*i.e.* kimberlites, lamproites, and lamprohyres) and presence in alluvial placers thought to be sourced from Proterozoic metaconglomerates (McCall, 2009) has precluded identifying a primary volcanic origin (Heaney et al., 2005). Bulk analyses of radiogenic lead isotopes implanted into carbonado diamond crystals combined with *in situ* analyses on inclusions hosted within the pore network yield crystallization ages ranging

from 3.8 to 2.6 Ga, with large uncertainties (Ozima and Tatsumoto, 1997; Sano et al., 2002). Basement underlying both the Central African Republic (Congo craton) and Brazil (São Francisco craton) are of similar lithology (Heaney et al., 2005) and age (2.6 to 2.0 Ga with enclaves as old as 3.55 to 3.0 Ga) (Haggerty, 2014), suggesting the possibility that carbonado formed during one event on a unified Archean landmass.

1.2.2 Diamond Material Properties

Several unusual characteristics distinguish carbonado from other varieties of diamond. Carbonado diamond structures exhibit a variety of textures, but are generally dense aggregates of randomly oriented crystals with edge lengths ranging from < 1 μm to 250 μm (De et al., 1998; Petrovsky et al., 2010; Piazolo et al., 2016). They are dominantly microporphyritic in texture with a bimodal crystal size distribution (De et al., 1998; Petrovsky et al., 2010). The larger, euhedral diamond crystals (10-250 μm) are "phenocrysts" in a cryptocrystalline, microdiamond (< 1μm) matrix. Most of the larger diamond phenocrysts are well-formed octahedra, but some show remnants of cubic growth, suggesting the first stage of diamond growth was physically and chemically optimal for diamond growth. The transition from cubic to octahedral growth implies a decrease in carbon supersaturation (Petrovsky et al., 2010). Throughout the microdiamond population of both African and Brazilian samples, De et al. (1998) observed exceptionally high dislocation densities ($> 10^{12}$ cm^{-2}), with subplanar dislocations interpreted as planar defect lamellae. The larger diamond crystals, however, are nearly dislocation free. Significant internal deformation has also been documented in the microdiamond population in a suite of African samples suggesting it is a common carbonado feature (Piazolo et al., 2016). Growth steps were only observed on the larger crystals, and dissolution features are absent (Petrovsky et al., 2010). Instead of a bimodal crystal distribution, Kaminsky et al. (2013)

found a log normal distribution from 1 to 55 μm with a mode at 6-8 μm in African and Brazilian samples. The lack of dissolution features for the larger diamond mode combined with a putative porphyritic texture suggest a perturbation of carbonado's growth environment leading to a sudden increase in nucleation rate. Other unusual features of carbonado the diamond include rare flow textures (Yokochi et al., 2008), columnar diamond growth (Rondeau et al., 2008), and vitreous external patinas on a single side of some samples.

1.2.3 Carbon Isotopic Composition

Carbonado is characterized by isotopically light carbon, with $\delta^{13}C$ values tightly clustered between -23 and -30 ‰ and two modes at -24 and -26 ‰ (De et al., 2001). Carbon isotopic values in diamonds worldwide span a large range from +5 to -41 ‰, but most (72%) fall between -2 and -8 ‰, which is similar to average mantle values. (Shirey et al., 2013). Variability of mantle carbon isotopic values has been attributed to a likely combination of primordial heterogeneities (Deines et al., 1993), fractionation processes (Stachel et al., 2009), and recycling of crustal carbon (Sobolev and Sobolev, 1980). This heterogeneity of mantle carbon is preserved in the two major parageneses of diamond: peridotitic and eclogitic. These paragenetic associations are based on the composition of silicate inclusions (mainly garnet and pyroxene), which are thought to reflect the nature of the host lithology in which the diamond grew. Peridotitic diamonds range from +0.2 to -26.4 ‰, but most fall within the modal diamond range (-2 to -8 ‰) (Cartigny, 2005). Eclogitic diamonds, however, span a larger range (+2.7 to -41.3 ‰) with lighter modes at -5 and -12 ‰ (De et al., 2001). While both parageneses include rare examples of carbonado-like values, the slightly lighter modal compositions of eclogitic diamonds may indicate formation in association with a lighter carbon source. There are few well

understood sources of carbon in the mantle that can produce values as light as those found in carbonado, with organic matter being the principal one.

1.2.4 Diamond Impurities

Carbonado diamonds vary in the abundance and composition of N, H, and fissiogenic impurities. Nitrogen concentrations fall between 18 to 1600 ppm (Shelkov et al., 1997; Yokochi et al., 2008) with the larger, euhedral diamonds usually having a lower relative concentration than the microdiamond matrix (De et al., 2001). Average whole carbonado $\delta^{15}N$ values are close to 0 ‰ (Yokochi et al., 2008) but can vary from 12.8 to -17 ‰ (Haggerty, 2014; Heaney et al., 2005). This range has been measured in typical monocrystalline diamonds worldwide and is largely decoupled from carbon isotopic compositions. Because sedimentary nitrogen, with $\delta^{15}N$ values > 0, is thought to undergo fractionation from degassing during subduction, it is difficult to use nitrogen isotopic values to trace reservoirs through the mantle. Nitrogen originally replaces carbon at single substitution sites because of nitrogen's slightly smaller ionic radius. Infrared spectrometry has been used to measure the extent of nitrogen substitution (aggregation states) in carbonado, which is linked to residence time in the mantle. Aggregation states in carbonado range from singly-substituted, non-aggregated nitrogen (Garai et al., 2006; Kagi and Fukura, 2008) to nitrogen platelets (Kagi et al., 1994) with the former being the more common state.. If diamond resides at mantle temperatures for a geologically long time (~0.5 to 3.0 Ga), the nitrogen atoms possess the necessary energy to diffuse through the diamond lattice to form doubly-occupied nitrogen sites (N2). With higher temperatures and longer residence times, even more advanced aggregation sites form as clusters of 4 nitrogen atoms per site or as platelets (Shirey et al., 2013). Aggregation states are determined using infrared spectrometry as different aggregation states absorb different wavelengths of IR

radiation. The presence of pervasive singly-substituted nitrogen in carbonado indicates a short (< ~ 100 Ma) residence time at mantle conditions (Kagi and Fukura, 2008). Hydrogen concentration and δD within the diamond material range from 40 to 100 ppm and from -130 to -200 ‰, respectively (Demény et al., 2011), which they claim are within the range of mantle values. Garai et al. (2006) identified hydrogen defects within the diamond material suggesting carbonado formed in a hydrogen-rich interstellar environment. Fissiogenic products from the radioactive decay of U (Xe, Kr, Ne, 4He, and implanted Pb) and K (^{40}Ar) occur in some samples (Ozima and Tatsumoto, 1997; Ozima et al., 1991). These products may be secondary, however, and related to the passage of fluids enriched in radioactive elements through the carbonado pore network (Ishibashi et al., 2016; Kagi et al., 2007; Rondeau et al., 2008).

1.2.5 Inclusion Suite

Carbonado lacks typical diamond mineral inclusions reflecting a mantle origin (e.g. pyrope, chromian clinopyroxene, pyrrhotite) (Heaney et al., 2005) and instead possesses an enigmatic inclusion suite that is unusually enriched in REE and actinides. Macro-inclusions filling or lining carbonado pore networks indicate equilibration at crustal P-T conditions, and evidently did not form at the pressures and temperatures required for diamond growth. Florencite, a hydrous REE-rich aluminophospate that commonly forms from the hydrothermal alteration of monazite is the most common mineral in the macro-inclusion suite (Trueb and De Wys, 1969, 1971). Several (~30) additional minerals have been identified, including kaolinite, quartz, and orthoclase (Heaney et al., 2005). Extensive acid leaching of whole carbonado samples can remove nearly all non-diamond phases (Dismukes et al., 1988; Kletetschka et al., 2000) suggesting that the pore network is largely open to exchange with the surface. Based on X-ray computed tomographic (XCT) imaging

of a single African sample, Ketcham and Koeberl (2013) suggested that macro-inclusions are compositionally heterogeneous, with replacement textures and diffuse and intergrown boundaries suggestive of local disequilibrium, and therefore macro-inclusions are likely secondary minerals formed by precipitation from fluids moving through a connected pore network during carbonado's residence at crustal conditions (Dismukes et al., 1988). Ketcham and Koeberl (2013) also identified pores with rhombic dodecahedral morphologies filled with florencite and kaolinite. Because this morphology is inconsistent with the crystal habit florencite and kaolinite, they interpreted these shapes to be the remnants of primary inclusions that have been replaced by the secondary mineral suite, while the pore geometries preserve the morphology of primary phases.

Contrary to the secondary nature of the macro-inclusion suite, TEM analyses have identified fully-enclosed nano-inclusions within individual diamond crystals interpreted to be syn- or proto-genetic. Most of these primary nano-inclusions are highly reduced native metals and alloys (i.e. Fe, Fe-Ni, Ni-Pt, Cr, Si, Ti, Sn, Ag, Cu, SiC, TiN), although other minerals (calcite, sylvite, garnet, ilmenite, phlogopite, and augite) and silicate-carbonate fluid inclusions have also been identified (De et al., 1998; Kaminsky et al., 2013; Sautter et al., 2011). The non-reduced nano-inclusion suite is stable only at typical upper mantle conditions and oxygen fugacity (wüstite/magnetite-fayalite/magnetite/quartz) (Sautter et al., 2011), whereas the reduced inclusions have been interpreted to form at a range of fO_2 values from 3 log units below the fayalite/magnetite/quartz buffer (Ishibashi et al., 2012) to 15 log units below the iron/wüstite buffer (Sautter et al., 2011). Interestingly, Sautter et al. (2011) found that reduced nano-inclusions only occur in the smaller microdiamond mode and, therefore, the drop in oxygen fugacity may have been a transient event. The nature of a redox buffer assemblage that can produce conditions as low as 15 log units below the iron/wüstite buffer remains unknown.

1.2.6 Porosity

Carbonado differs from other varieties of polycrystalline diamond (*i.e.* ballas, bort, and framesite) by hosting an extensive network of interconnected pores and this unusual characteristic must be accounted for in models of carbonado genesis. Retention of primary effective porosity within carbonado can be excluded because of the intense pressure required for diamond crystallization. Thus, it seems likely that other mineral phase(s) occupied carbonado pore space while at diamond-forming pressures. While carbonado pore networks have long been recognized, few studies have characterized their 3-D geometries. Trueb and Butterman (1969) and Trueb and De Wys (1969, 1971) imaged African and Brazilian samples using X-ray radiography and noted a preferred orientation of elongated pores. Forty years later, Ketcham and Koeberl (2013) documented similar pore textures and shapes, with non-uniform pore distributions and layers of pores spatially related to a patinaed surface.

1.2.7 Genetic Theories

Theories proposed for carbonado diamond formation fall into three diverse categories: crustal, extra-terrestrial, and mantle.

- Smith and Dawson (1985) suggested carbonado's isotopic similarity to organic carbon and lack of typical mantle inclusions could be explained by an extra-terrestrial impact into an organic carbon-rich. However, lonsdaleite, an allotrope of carbon associated with confirmed impact diamonds and diamond aggregates, has never been reported in carbonado (Trueb and De Wys, 1969, 1971). Furthermore, although carbonado "phenocrysts" have dimensions similar to the micron size of most impact

diamonds (Shirey et al., 2014), no mechanism for sintering them together has been proposed.

- Ozima et al. (1991) and Ozima and Tatsumota (1997) measured fissiogenic isotopes (Pb, Xe, Kr, Ne, and He) implanted into the diamond crystals from the spontaneous fission of uranium. An excess of these fission products relative to the concentration of uranium in pore network material led them to hypothesize that carbonado formed from irradiation of carbonaceous material in the upper crust. However, uranium could instead have been lost from the pore network. Furthermore, diamonds formed through irradiation have nanometer sizes and, again, no mechanism for sintering them together has been proposed.
- Similarity of rare earth patterns from acid-leachates of carbonado pore-filling material to crustal material has supported crustal origin theories for carbonado formation (Kamioka et al., 1996; Shibata et al., 1993). Shibata et al. (1993) measured whole carbonado using instrumental neutron activation analysis, but many elements were near or below detection limits. Kamioka et al., (1996) also analyzed whole carbonado using INAA, but did not remove surface contaminants.
- Garai et al. (2006) and Haggerty (2014) argue for a hydrogen-rich interstellar origin, possibly from the core of a white dwarf or carbon exoplanet, based on FTIR spectra revealing hydrogen defects within diamond material and the presence of extremely reduced nano-inclusions. However, it is extremely unlikely that material formed in a different solar system would have isotopic ranges of C, N, and H that coincide with terrestrial values. Also, the silicate minerals (e.g. phlogopite, augite, and

ilmenite) and fluid inclusions that have been documented within the diamond phenocrysts, which would not form in a H-rich environment.

- More recently, genetic theories have converged towards a mantle origin, likely involving fluids supersaturated in carbon and rich in incompatible elements. Because of recent advances in micro-analytical techniques, mineral and fluid inclusions suggestive of growth in such an environment have been documented as inclusions within the diamond "phenocrysts". Higher resolution images of diamond growth morphologies and 3-D imaging of carbonado have also corroborated this theory. Several authors propose a two-stage process with a rapid increase in nucleation rate from a transition in P-T-fO_2 produced the putative bimodal crystal size distribution (Ishibashi et al., 2012; Ketcham and Koeberl, 2013; Petrovsky et al., 2010).

1.3 GOAL OF THIS STUDY AND HYPOTHESES

The present study extends XCT analyses to a large number (25) of carbonado specimens, to determine whether the internal textures identified in a single sample by Ketcham and Koeberl (2013) are intrinsic to carbonado, and to document other textures that may bear on carbonado genesis. To test the hypothesis that the present-day mineral assemblage formed from the *in situ* breakdown of primary phases, we document internal textures of pores and ICP-MS elemental compositions of leachable pore-filling material. To evaluate the effectiveness of whole-sample acid-leaching on carbonado, we image specimens before and after acid treatment. Finally, we discuss the implications of our results in the context of carbonado genesis in a mantle environment that represents a new endmember of the diamond-forming spectrum.

Chapter 2: Insights into Internal Textures Using X-ray Computed Tomography

2.1 INTRODUCTION

Because carbonado diamond is one of the hardest natural substances, most studies have been limited to small pieces that are powdered, fractured, focused ion beam (FIB)-extracted, laser-cut, or laboriously polished. These techniques provide a spatially limited, two-dimensional perspective from which it is difficult or impractical to relate macro-inclusions, pore textures, and other features to one another. Ketcham and Koeberl (2013) demonstrated the added value of XCT for characterizing the 3-D distributions of pores and pore fabrics, and we perform similar analyses in a new and larger carbonado data set. Based on these analyses, a subset of samples are then subjected to a sequential acid leaching process, and the leachates analyzed for elemental concentrations by ICP-MS to understand the compositions of pore-filling materials and how, along with XCT textural information, they may relate to carbonado diamond formation

2.2 SAMPLES IN THIS STUDY

Twenty-five carbonado samples, totaling 350 carats, from both the Central African Republic and Brazil were obtained for this study (Table 2.1). Several African samples (C-16-A through E) were purchased from a commercial dealer, and two large specimens were obtained on loan from the Natural History Museum, Vienna (N628 and M8348). The 23-carat African sample analyzed by Ketcham and Koeberl (2013) was also included in this study (K+K). Brazilian samples from placers near the municipalities of Andaraì and Lençóis (Bahia state) and near Rio Macaúbas (Minas Gerais state) were unused specimens from the study by Sano et al. (2002), provided by M. L. Chaves. Samples in the composite carbonado study set range from 1.66 carats (0.33 g, ~ 8 mm × 5 mm × 4 mm) to 141 carats

(28.2 g, ~ 45 mm × 23 mm × 20 mm), with most < 10 carats. They are irregularly shaped and with rounded to angular edges and smooth to rough surfaces and variable pore densities that are visible to the naked eye. They exhibit a variety of colors (from brown to silver to black) and lusters (from dull to vitreous). Figure 2.1 illustrates this diversity of carbonado exteriors.

Table 2.1 Sample Information and Scanning Parameters

Sample	Location	Mass (g)	Mass (ct)	Energy (kV)	Scan Time (hr)	Voxel Size (µm)	Total Slices
C-16-A	CAR	4.58	22.91	80	1.2	19.5	843
				140	2.0	3.8	935
C-16-B	CAR	0.74	3.69	80	1.4	14.4	462
				140	1.5	4.4	935
C-16-C	CAR	0.71	3.57	80	1.8	14.4	448
				140	4.0	2.0	986
C-16-D	CAR	0.69	3.47	80	1.2	14.4	431
				140	3.0	2.0	986
C-16-E	CAR	0.62	3.09	80	1.2	14.4	489
				140	3.0	2.7	995
1-1	RM	1.46	7.29	80	1.1	19.8	734
1-2	RM	0.98	4.89	80	1.1	19.8	734
1-3	RM	1.00	5.01	80	1.1	19.8	734
					1.2	14.4	815
1-6	RM	0.42	2.11	80	1.1	19.8	734
					1.2	14.4	828
1-7	RM	0.44	2.22	80	1.1	19.8	734
2-8	And	1.82	9.11	80	0.9	24.5	864
2-9	And	1.75	8.73	80	0.9	24.5	864
2-10	And	1.34	6.70	80	0.9	24.5	864
2-11	And	0.33	1.66	80	0.9	24.5	864
					1.2	14.4	828
2-12	And	1.03	5.15	80	0.9	24.5	864
3-13	Len	0.91	4.55	80	1.1	22.2	821
3-14	Len	0.68	3.39	80	1.1	22.2	821
3-15	Len	1.45	7.26	80	1.1	22.2	821
					1.4	14.4	729
					2.8	4.0	945
3-16	Len	1.15	5.76	80	1.1	22.2	821
3-17	Len	1.96	9.81	80	1.1	22.2	821
3-18	Len	0.62	3.09	80	1.1	22.2	821
					1.1	14.4	625
3-19	Len	0.49	2.47	80	1.1	22.2	821
N628	Unknown	11.97	59.85	40	6.3	24.4	840
				140	1.3	24.4	841
M8348	CAR	28.20	141.00	40	5.3	53.7	852
				140	1.6	53.7	858
				140	4.2	4.5	934
K+K	CAR	4.60	23.00	40	0.8	27.3	1014
				60	2.3	5.5	994

(CAR)-Central African Republic; (RM)-Rio Macaúbas, Brazil; (And)-Andaraì, Brazil; (Len)- Lençóis, Brazil

Figure 2.1 Stereomicroscope Images of Carbonado Exterior

All scale bars are 1 mm and sample names are in the lower right corner of each image

2.3 METHODS

2.3.1 X-ray Computed Tomography (XCT) Scanning Procedures

Samples were imaged using the Zeiss MicroXCT scanner at the University of Texas High Resolution X-ray CT Facility (UTCT). XCT produces a continuous sequence of two-dimensional (2D) 16-bit grayscale images (slices), which when stacked together create three-dimensional (3D) volumes. Each voxel (a pixel with volume) is assigned a grayscale value proportional to the average X-ray attenuation of the material comprising that voxel. X-ray attenuation is a function of a material's atomic number and density, as well as the X-ray energy; denser, more attenuating material is typically assigned a brighter grayscale value (Ketcham and Carlson, 2001). Scanning resolutions are reported in terms of voxel dimensions; a scanning resolution of 14.35 μm/voxel, for example, corresponds to a cube with edge lengths 14.35 μm long. After scanning, X-ray density images for each 2D carbonado slice were assembled into 1000 × 1000 16-bit grayscale images, with up to 1014 "slice-images" for the largest specimen. Software corrections were applied to compensate for ring and beam hardening artifacts. 3-D renderings of carbonado density contrasts were generated from 16-bit grayscale images using Avizo™ (Version 9.3) to assist in volumetric visualization. The application of XCT enables 3-D rendering of solid versus pore space, as well as spatial and compositional differentiation of constituent solid phases.

African samples were initially scanned individually (Table 2.1), but because of the large number of Brazilian samples, the specimens from each locality were grouped together and imaged in a single scan, with resolutions at 25 μm/voxel compared to the ~14.35 μm/voxel resolutions used for the African samples. Samples of interest with any pore textures, shapes, distributions, or features that we wanted to observe at higher magnifications and resolutions were then selected to be scanned individually. Most initial

scans were performed at 80 kV, except N628 and M8348, which were scanned at 40 and 140 kV in attempts to track the distribution of high-atomic-number phases, which will attenuate X-rays more at the higher energy scans. The MicroXCT scanner design allows us to magnify regions of interest within a sample, in a manner analogous to switching objectives on a petrographic microscope, to image targeted subvolumes with resolutions down to 1.77 μm/voxel. These higher-resolution images were scanned at 140 kV.

2.3.2 Analysis of Individual Pores Using Blob3D

Carbonado literature is replete with the term "pore" to define any non-diamond volume within a carbonado specimen. Volumes filled/lined with crustal minerals are stilled called pores even though it is contrary to the notion that a pore is an empty void. We maintain this nomenclature and call any non-diamond volume within a sample a pore. Measurements of individual pores, both empty and filled, were made using Blob3D software (Ketcham, 2005a). Whole-sample volumes were used for all assessments of pores except K+K, where a representative subvolume was selected based on similarity of pore shape, size, distribution, and filling material compared to the rest of the sample. In Blob3D processing, objects of interest are isolated from the data volume by assigning grayscale threshold values (Figure 2.2). Grayscale threshold ranges were unique for every specimen and selected to most accurately represent the largest number of pores within the sample (Appendix A). Threshold values greater than the diamond matrix were used for samples where most pores are filled with brighter (higher atomic density) material, whereas values less than the diamond matrix were used for samples mainly possessing empty pores.

Three-dimensionally contiguous voxels matching the same grayscale threshold are grouped as one object termed a blob. Next, individual blobs are then examined to manually separate touching or impinging objects. Carbonado's pore network is complex with

thousands of pores per sample varying in size, shape, and filling material. At the resolution used for Blob3D analysis, dense clusters of pores are seemingly connected, whereas some individual pores were isolated. Because of the pore network's complexity, not every segmented blob is an accurate 3-D representation of the actual pore in the XCT data. Blobs smaller than 50 voxels, connected to the exterior of the sample, or unrepresentative of the real shape (often caused by polymineralic inclusions with material outside the grayscale threshold), as determined by the analyst, were excluded from measurement. Also, because we were interested in measuring individual pores, any clusters of connected blobs (> ~ 5 blobs) that could not be objectively separated with the tools provided in Blob3D were excluded as well. Several factors can cause individual pores to be grouped into one blob: (1) densely clustered pores that were actually connected; (2) image artifacts from nearby highly-attenuating phases; (3) non-diamond material in pores or along grain boundaries below the limits of detection increasing the overall grayscale value of the diamond matrix, making the surrounding pores appear to be connected. While thousands of blobs were segmented in each sample, most could be immediately discarded because they met one of the aforementioned exclusion criteria. After all processing was complete, less than 10% of the segmented blobs were accepted and measured. However, the retained blobs are a representative subset and useful for measuring the shape, size, and orientation of pores in carbonado.

After isolating and examining every individual blob volume, ellipsoid dimensions that best-fit the retained blob volumes were extracted. Orientations of long and short axes were plotted on stereonets using Stereo32 software (Roeller and Trepmann, 2010), which also calculates the fabric type (K) and strength (C) (Woodcock and Naylor, 1983), with higher C values corresponding to stronger, less random fabrics.

Figure 2.2 Fundamentals of Blob3D

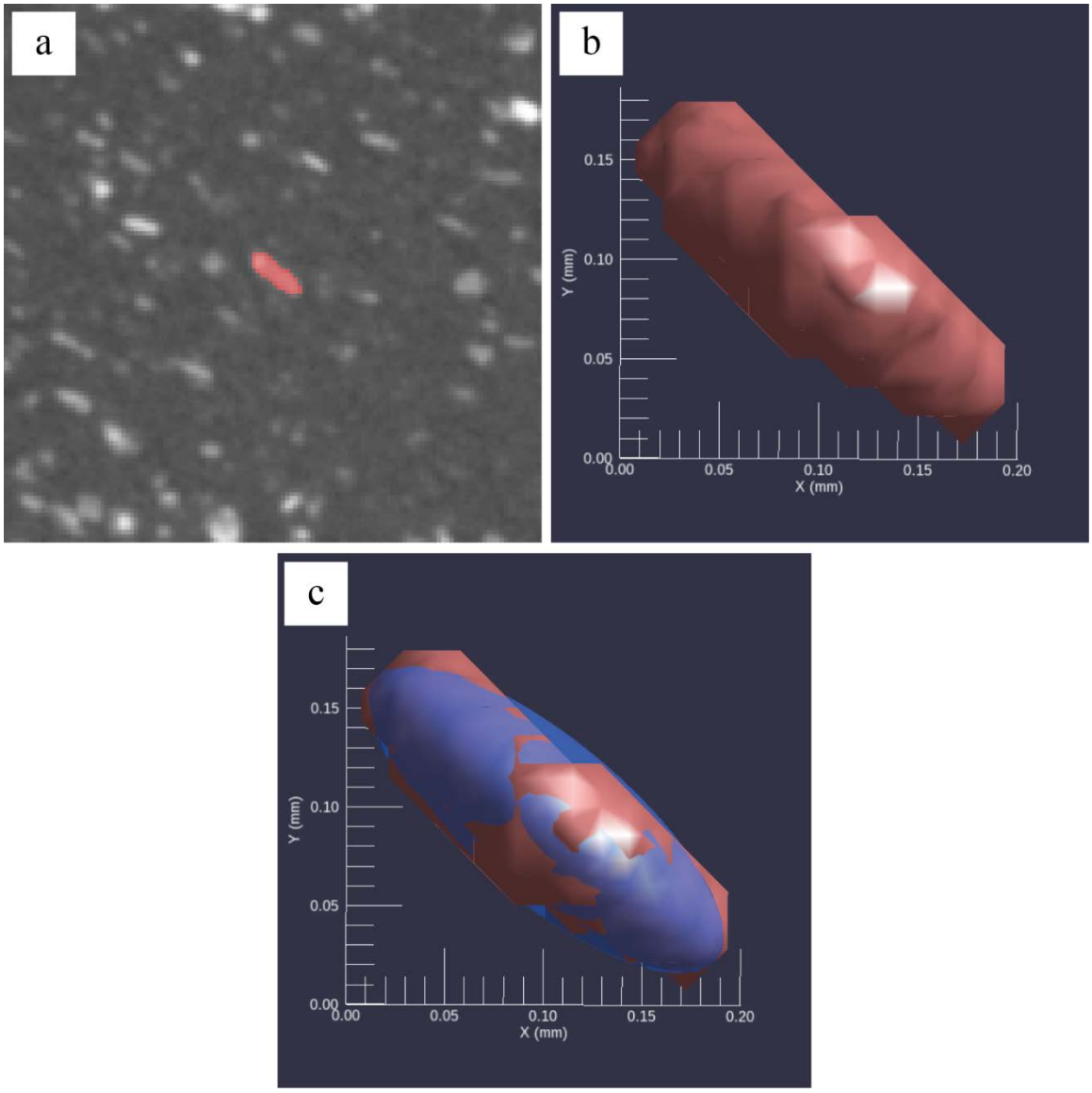

(a): Grayscale threshold values are determined for the component of interest (pores). (b): Contiguous sets of voxels that meet these criteria (blobs) are segmented from the data volume. (c): Dimensions of best-fit ellipsoids are extracted.

2.3.3 Fabric Analysis Using Quant3D

In addition to Blob3D, Quant3D software (Ketcham, 2005b) performs a fabric analysis on the whole volume in a fraction of the time (< 10 minutes compared to hours per sample using Blob3D). The main distinction is that Quant3D quantifies the fabric as a continuum, rather than as a set of discrete objects. We used star volume distribution (SVD) analysis, included in the Quant3D package, to determine whether pores had a preferred orientation. This calculation is based on principal component directions and magnitudes and shape indices of the objects that meet a particular grayscale threshold. Grayscale ranges, which were different from those used for Blob3D, were determined by the analyst to represent the largest number of pores. The software generates a 3-D rose diagram to visualize the data.

2.3.4 Application of Textural Analysis to Framesite Diamond

Because these are the first generated 3-D textural data for a suite of carbonado diamonds, we also analyzed the pores of a framesite diamond to provide context for our measured fabrics. The framesite XCT data were collected at Johannes Gutenberg University Mainz in an earlier study by Jacob et al. (2011). Framesite is a less porous (~ 1.5 %) polycrystalline diamond variety found in kimberlites, thought to crystallize from the redox reaction between a carbon supersaturated fluid and the reduced lithospheric mantle shortly before eruption (Jacob et al., 2011).

2.4 RESULTS

2.4.1 New Categories for Carbonado Based on XCT Observations

Analyzed carbonado specimens can be divided into three categories based on the degree to which pores are filled with non-diamond material: filled, intermediate, and

unfilled. The “filled” variety likely contain the macro-inclusion suite of minerals that may have equilibrated at crustal conditions, as suggested by Ketcham and Koeberl (2013) in their analysis on sample K+K (Figure 2.3). This interpretation is based on replacement textures and diffuse, intergrown boundaries between phases with contrasting X-ray attenuation comprising individual pores. Disseminated highly-attenuating phases are pervasive and likely the same REE-rich material interpreted by Ketcham and Koeberl (2013). This heterogeneous and unequilibrated composite either completely fills or rims > 99% of the identifiable pores in the filled variety. The relatively few unfilled pores occur both near the surface and in the deeper interior, with no obvious spatial relationship to other features (*e.g.* patinaed surface and healed fractures). Their size, shape, and apparent orientation, at least in the XCT data, are similar to the filled pores, suggesting dissolution of previous material or that they are primary and were never infilled. The aforementioned replacement textures identified by Ketcham and Koeberl (2013) occur in nearly all samples at the individual pore scale, and highly attenuating material that was interpreted as REE-rich phases, is randomly distributed throughout samples.

The “unfilled” variety of carbonado specimens, however, is dominated by empty pores but may have filled pores that are directly connected to the surface. Unlike the “filled” variety’s macro-inclusion suite, the “unfilled” variety can have isolated, highly-attenuating, nearly spherical material completely filling or lining individual pores, but these are sparsely distributed (Figure 2.4). Less attenuating inclusions that are compositionally more homogeneous than pores in “filled” specimens are located toward sample edges, implying they may be altered versions of the bright inclusions or precipitated during carbonado’s residence in the upper crust. In general, the unfilled pores have the appearance of sharper boundaries, likely because they do not contain material that scatters x-rays more than the diamond matrix.

The intermediate samples, C-16-D and N628, (Figure 2.5) are unique because they have both filled/lined and unfilled pores. The filled/lined pores form a coherent and isolated 3D volume of pores with similarly attenuating material sharply juxtaposed with sample volumes occupied by empty pores. Contrary to the heterogeneous composite found in individual pores in the "filled" samples, the filling/lining material in these samples is more compositionally homogeneous based on observations of XCT data. While these samples have filled pores near the surface, the coherent interior domains are not recognizably associated with the sample edges.

Two end-member scenarios can be posed for this texture: the filled domains may represent undissolved primary phases, or they may be secondary phases following dissolution of primary phases in some or all pores. If the pore-filling material formed by precipitation in association with percolating fluids, it seems unlikely that exterior pores would be unaffected compared to deeper pores. It may be more plausible that filled domains represent undissolved material or altered interior material that has only migrated a limited distance, as evidenced by sharp boundaries delineating the filled domains. However, more complex scenarios involving multiple episodes of dissolution and precipitation cannot be ruled out. High-density phases with the same morphology and distribution as the material in the unfilled carbonado variety are located in the interior of these samples. Thus, this texture may represent an intermediate variety between filled and unfilled.

Figure 2.3 XCT Images of a Filled Sample

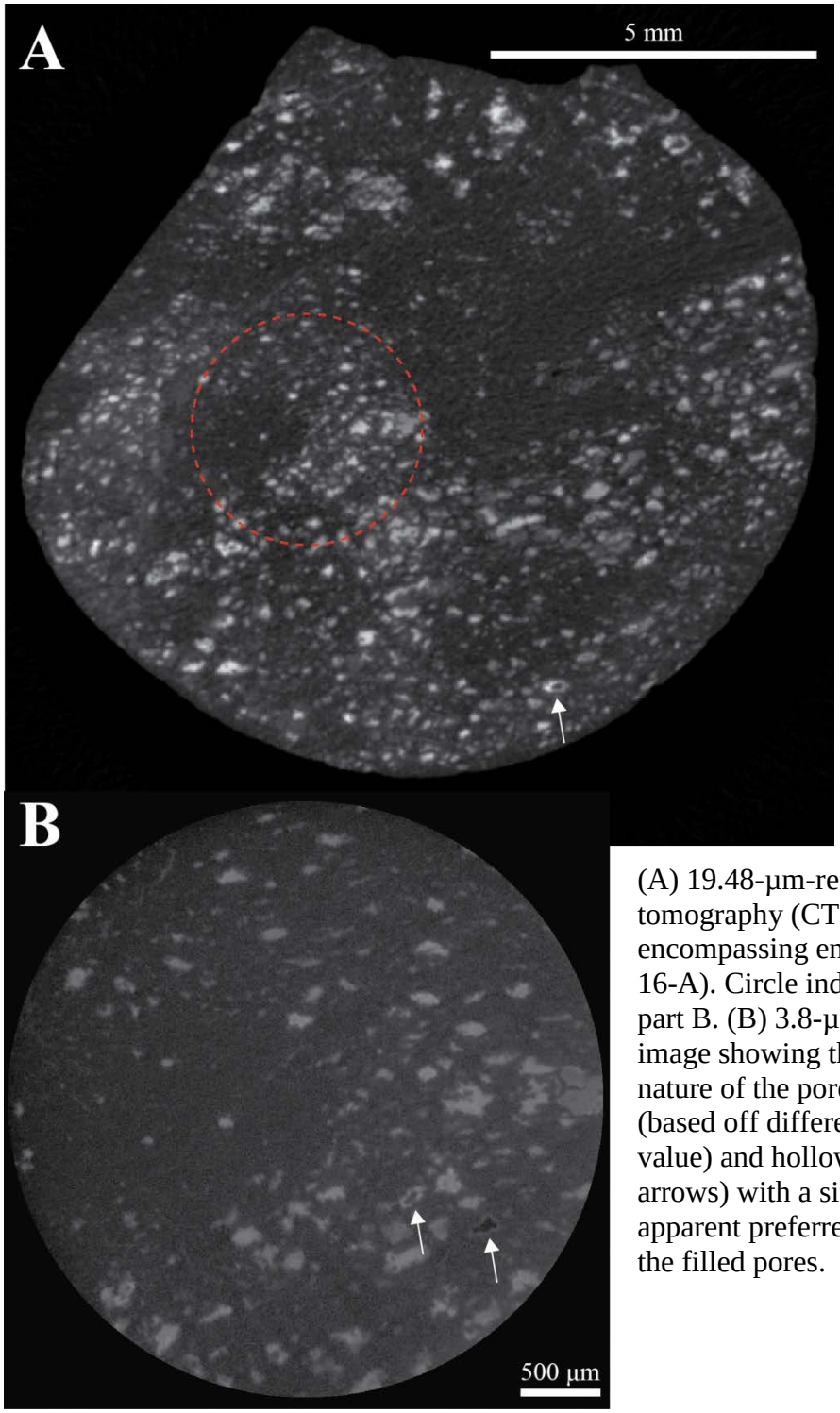

(A) 19.48-µm-resolution computed tomography (CT) image encompassing entire specimen (C-16-A). Circle indicates position of part B. (B) 3.8-µm-resolution image showing the heterogeneous nature of the pore-filling material (based off differences in grayscale value) and hollow pores (white arrows) with a similar shape and apparent preferred orientation as the filled pores.

Figure 2.4 XCT Image and Volume Rendering of an Empty Sample

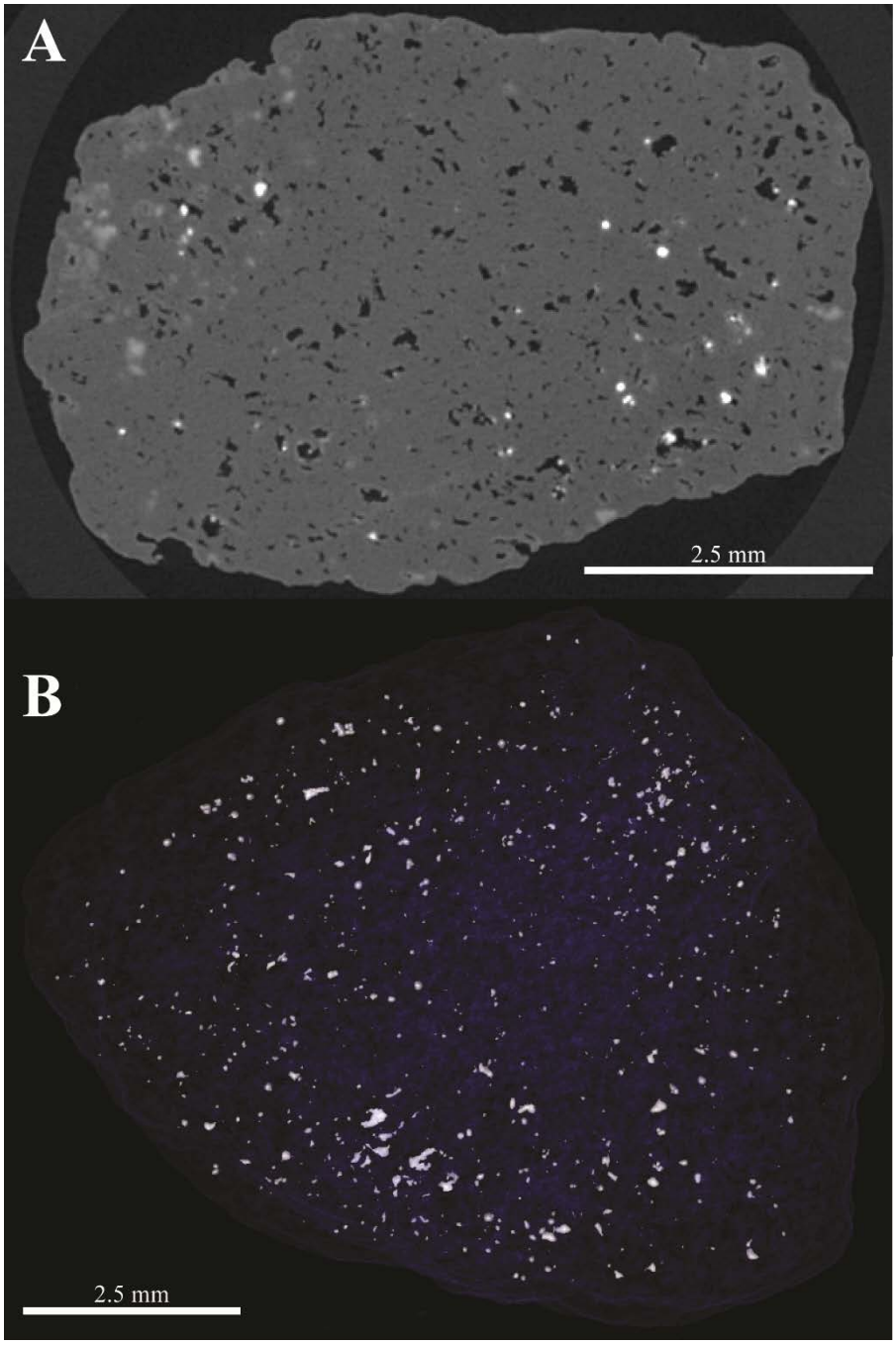

(A) 14.35-µm-resolution image encompassing entire specimen (3-18) showing mostly empty pores with isolated and highly-attenuating material of variable sphericity sparsely distributed throughout. (B) Volume rendering from the 14.35-µm-resolution dataset showing the highly-attenuating inclusions relative to the diamond matrix. Diamond is rendered transparent blue.

Figure 2.5 XCT Images of Partially Filled Samples

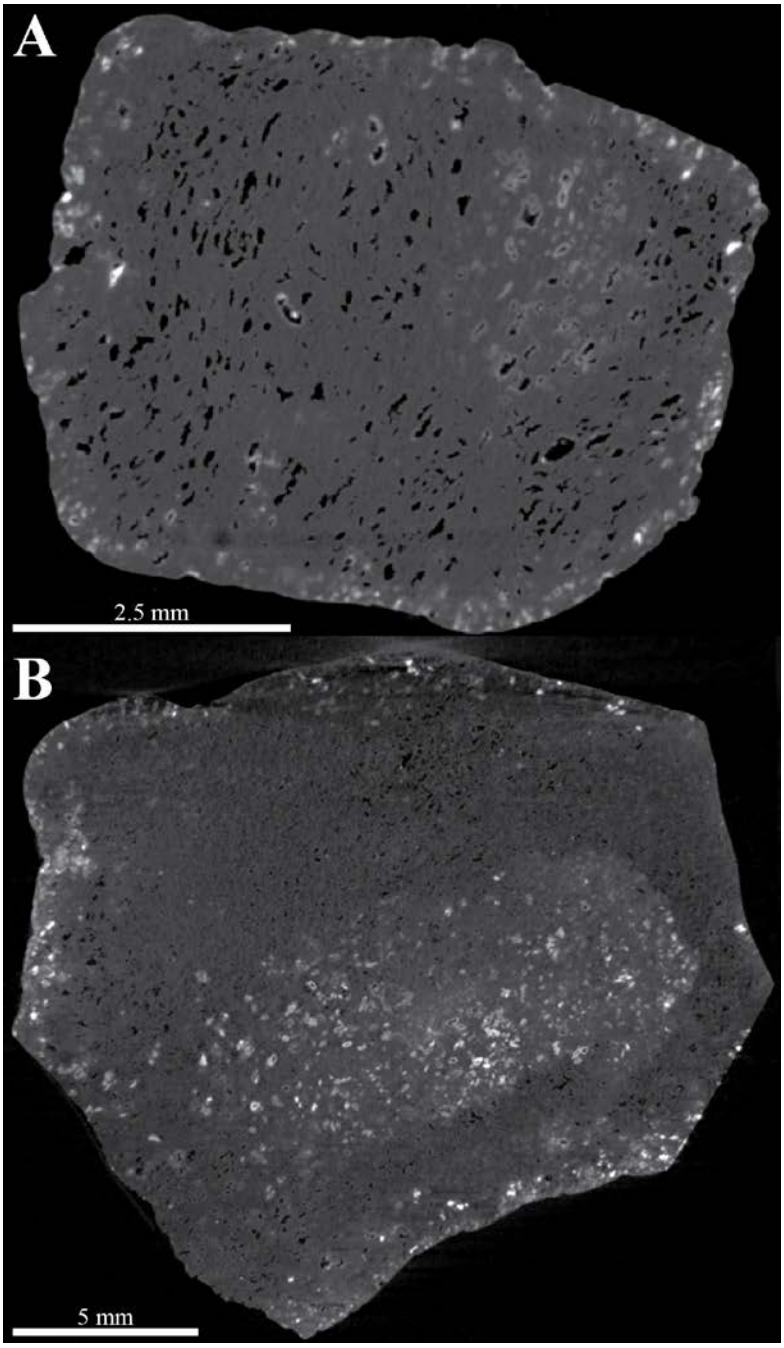

(A) 14.36-µm-resolution image encompassing entire specimen (C-16-D) and (B) 24.37-µm-resolution image encompassing entire specimen (N628) showing filled and unfilled pores and interior regions with similarly attenuating pore-filling material sharply juxtaposed to regions with empty pores. These samples are largely rimmed by filled pores.

2.4.2 Remnants of Primary Crystalline Phases

While most pores are irregularly shaped, some have unusually flat edges that meet at sharp angles on one or more sides suggestive of a crystal habit but whose overall shapes are still anhedral, precluding positively identifying them as remnant clues of primary minerals. However, C-16-D, a mostly unfilled sample features an empty cavity that can unambiguously be identified as originating from a primary crystalline phase (Figure 2.6). Unlike the euhedral pseudomorphs identified by Ketcham and Koeberl (2013), this pore appears to represent a primary mineral that was partially resorbed during diamond growth, evidenced by rounded vertices and diamond ingrowths, making determining its crystal habit difficult. It is not rhombic dodecahedral, like those identified by Ketcham and Koeberl (2013), and thus likely represents a different phase. By measuring a 3D volume rendering, we determined that its axes' lengths are ~ a = 580 μm; b = 1000 μm; c = 1500 μm but cannot definitively measure the angle between them. Based on axis length alone, we can speculate that it was an orthorhombic, monoclinic, or triclinic mineral. In general, euhedral shapes that can be unambiguously interpreted as remnants of primary crystalline phases are rare in carbonado.

Figure 2.6 Orthogonal XCT Images Showing the Cavity of a Primary Euhedral Inclusion

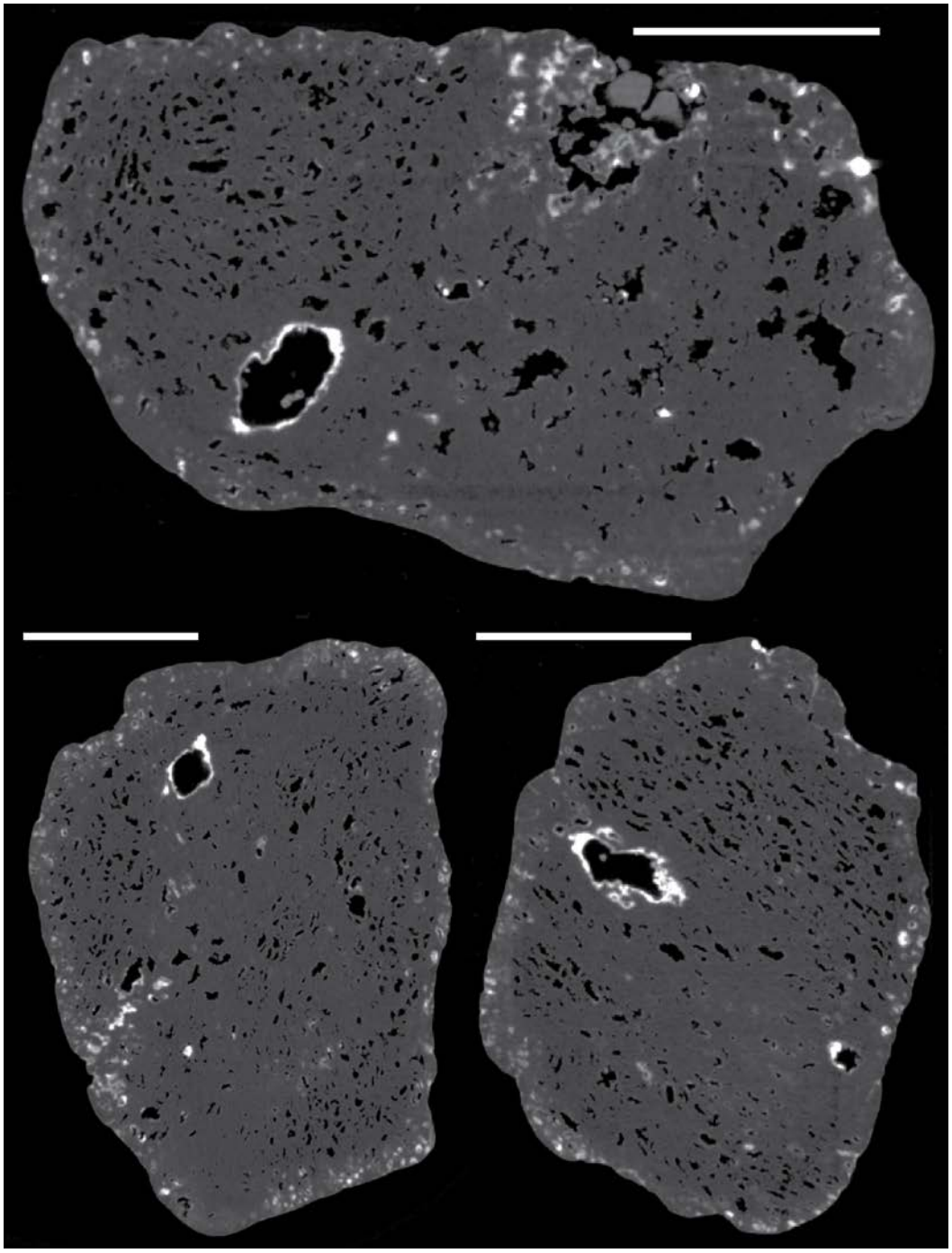

14.36-µm-resolution images along orthogonal axes encompassing entire specimen (C-16-D) showing cavity interpreted to be a primary crystalline phase (large hollow cavity lined with bright material) that was partially resorbed during diamond growth. Scale bar for all images is 2.5 mm.

2.4.3 Other Textural Observations

Pore distribution and density varies among samples and within individual specimens. Figure 2.7 demonstrates textures characterized by uniform pore distributions throughout samples C-16-C and 1-3, with the former having a greater density of pores. Figure 2.8 is a single XCT slice of a scan encompassing four samples that shows a variety of non-uniform pore textures in other carbonado specimens. Samples 3-15 and 3-16 have non-uniform pore distributions. In sample 3-15, two regions of contrasting pore distribution, density, and orientation are separated by a ~1 mm thick planar zone that is largely free of pores (Figures 2.8 and 2.9). These contrasts are also visible on the sample surface to the naked eye. These contrasting regions also have distinct boundaries with the pore-free plane separating them. The top right region of 3-15 in Figure 2.8 sharply juxtaposes the pore-free plane while the bottom left volume has a gradation of increasing pore density away from the plane. Similar volumes of contrasting pore distribution and density are randomly located in other specimens with no spatial relationship to other features and can have sharp or diffuse boundaries. Also, healed fractures are common, but these cross-cut all features and must be late-stage features (Figure 2.8).

Figure 2.7 XCT Images Illustrating Uniform Pore Distribution

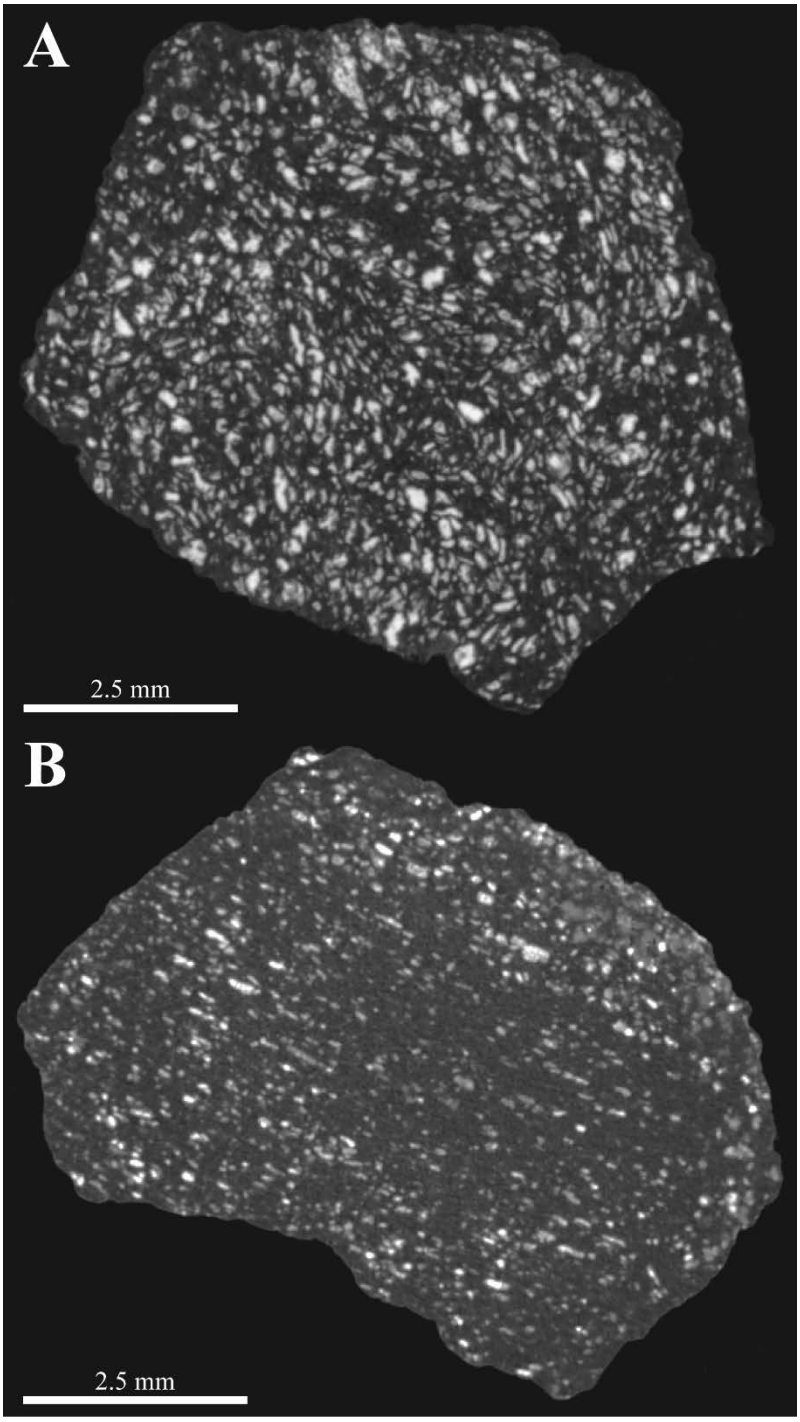

(A) 14.36-µm-resolution image encompassing entire specimen (C-16-C) and (B) 14.35-µm-resolution image encompassing entire specimen (1-3) showing evenly distributed pores throughout specimens. C-16-C, however, has a greater pore density.

Figure 2.8 XCT Image Illustrating Textural Diversity in Carbonado

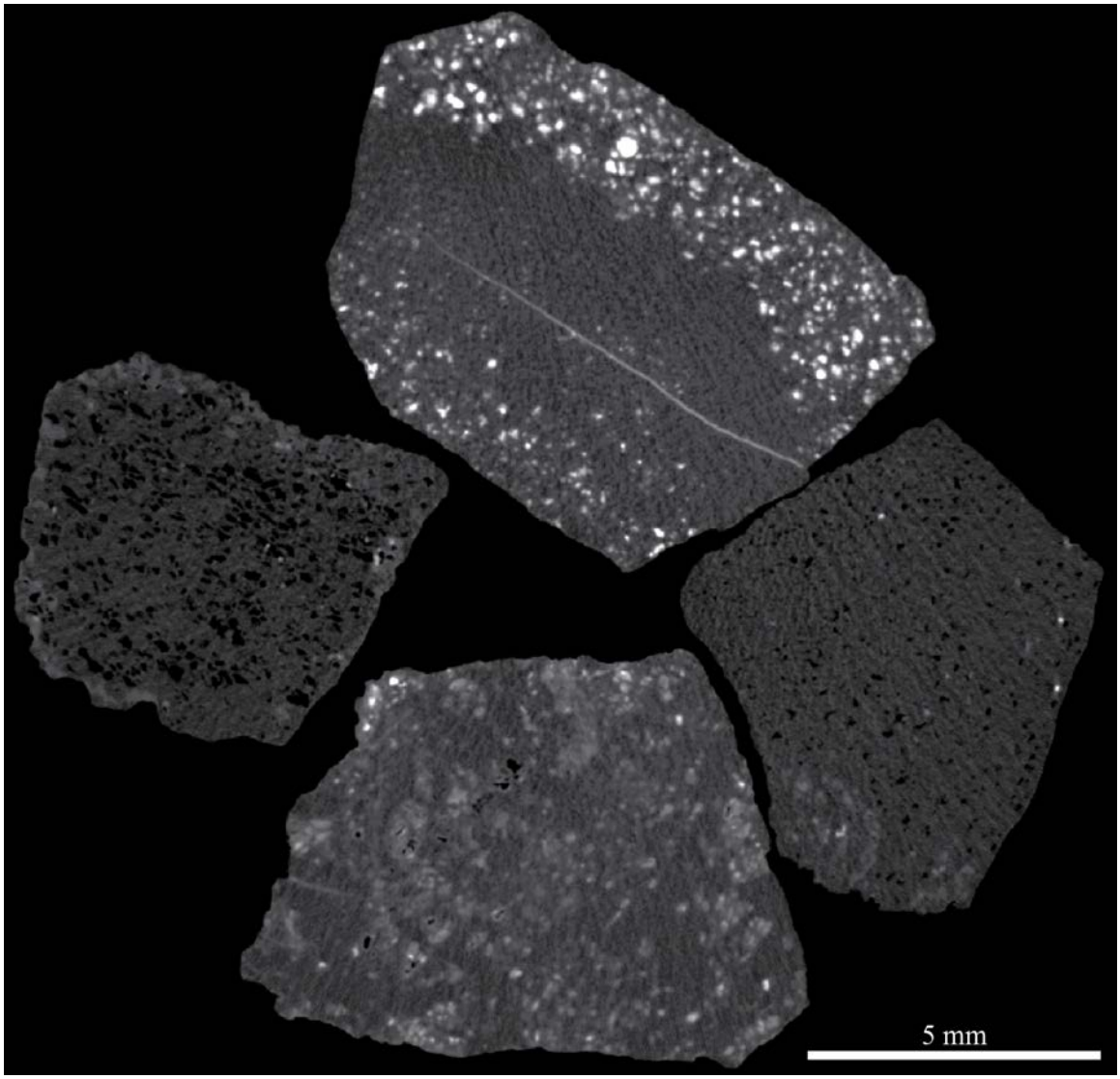

22.17-µm-resolution image encompassing 3-13 (right), 3-14 (left), 3-15 (top), and 3-16 (bottom) illustrating examples of textural diversity that exists among carbonado samples. Both 3-13 and 3-14 have empty pores, but the pores in 3-14 are larger. 3-15 and 3-16 show non-uniform pore distributions and variable pore densities. 3-15 has a distinct plane almost 1 mm wide mostly free of pores. 3-16 shows cloudy regions where non-diamond material likely exists in grain boundaries or pores below the resolution of the CT scan.

Figure 2.9 Pore-free Plane

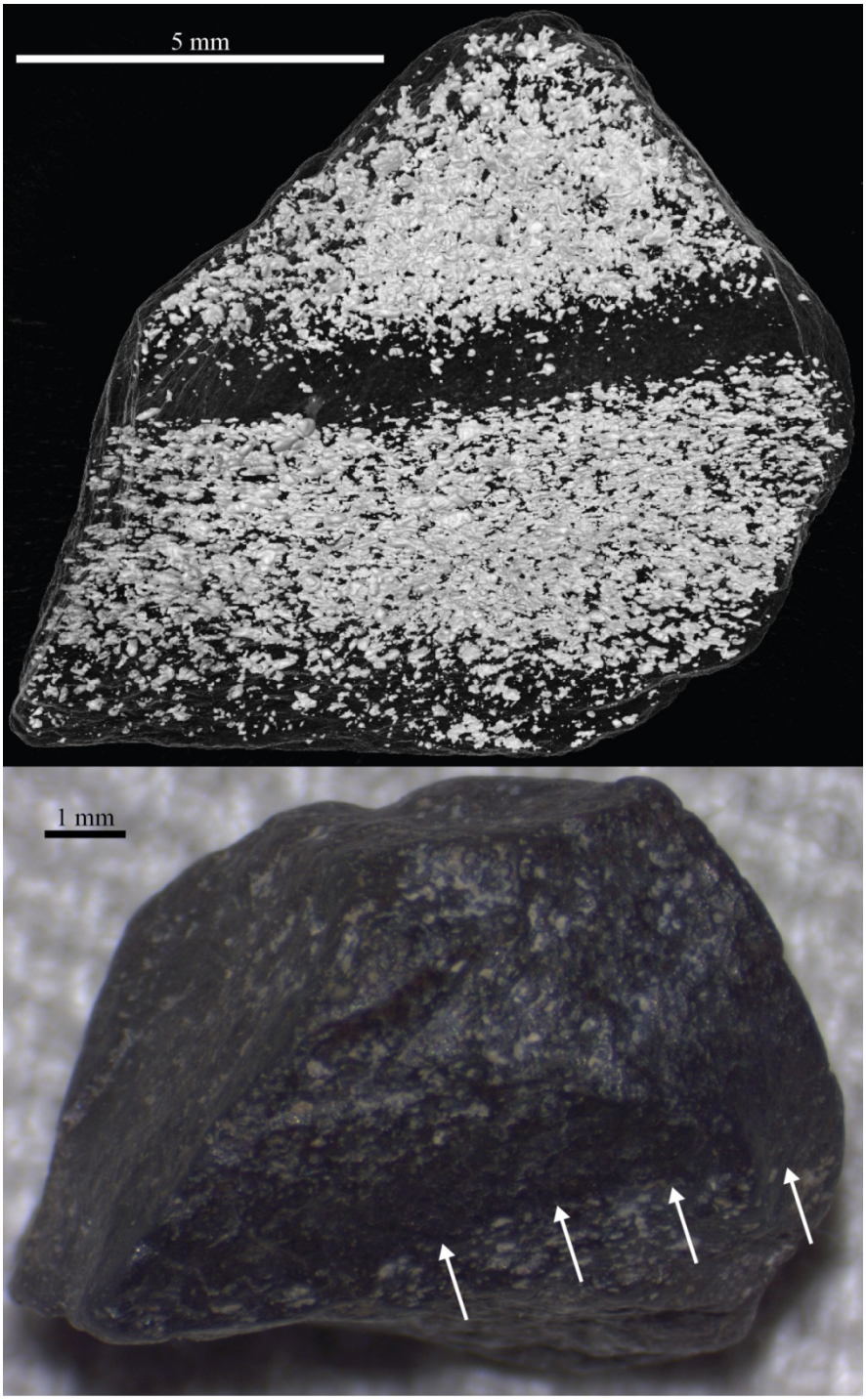

Volume rendering from 14.35-µm-resolution data and stereomicroscope image for 3-15 showing the ~ 1 mm thick planar zone mostly free of pores that extends across the entire specimen. Diamond material is rendered transparent.

2.4.4 Pore Size Distributions

The average volume of individual pores (Table 2.2) within samples spans an order of magnitude (0.0004 mm^3 to 0.004278 mm^3). These volumes correspond to equivalent sphere diameters of 91 µm and 201 µm, respectively. This variation may arise from scanning resolution effects. With higher resolution scans, smaller pores are more easily resolved, expanding the pore size distribution to lower values. Furthermore, the ability to identify and measure pores is also heavily influenced by the filling material. Empty pores or ones filled with material significantly more attenuating than diamond are more easily resolved. If the filling material attenuates X-rays similarly to diamond, then the pore may be unidentifiable or appear smaller than it really is. The lower values are for sample K+K, which has a pore distribution spanning a larger range, but with a lower average (Figure 2.10). However, measurements on K+K were performed on higher resolution data compared to other analyses. This sample also contains larger pores (Ketcham and Koeberl, 2013), but they were not measured due to their heterogeneous filing complicating processing them accurately as single objects. Nevertheless, all of our average measured pore-volumes are two to three orders of magnitude larger than our framesite analysis, reflecting a fundamental difference in the amount and size of pores between the two species of diamond.

Table 2.2 Average Best-Fit Ellipsoid Values from Blob3D

	Axis Lengths (μm)				# of ellipsoids	
	Long	Intermediate	Short	Aspect Ratio	measured	Pore Type
C-16-A	291	201	135	2.2	1095	Filled
C-16-B	269	182	113	2.4	465	Filled
C-16-C	248	169	107	2.3	663	Filled
C-16-D	263	175	98	2.7	753	Empty
C-16-E	196	131	79	2.5	684	Filled
K+K	140	92	58	2.4	870	Filled
1-3	194	137	89	2.2	302	Filled
2-11	236	164	89	2.7	425	Empty
3-15	230	164	95	2.4	200	Filled
Framesite	41	25	14	2.9	130	Empty

Figure 2.10 Pore Size Distributions from Blob3D

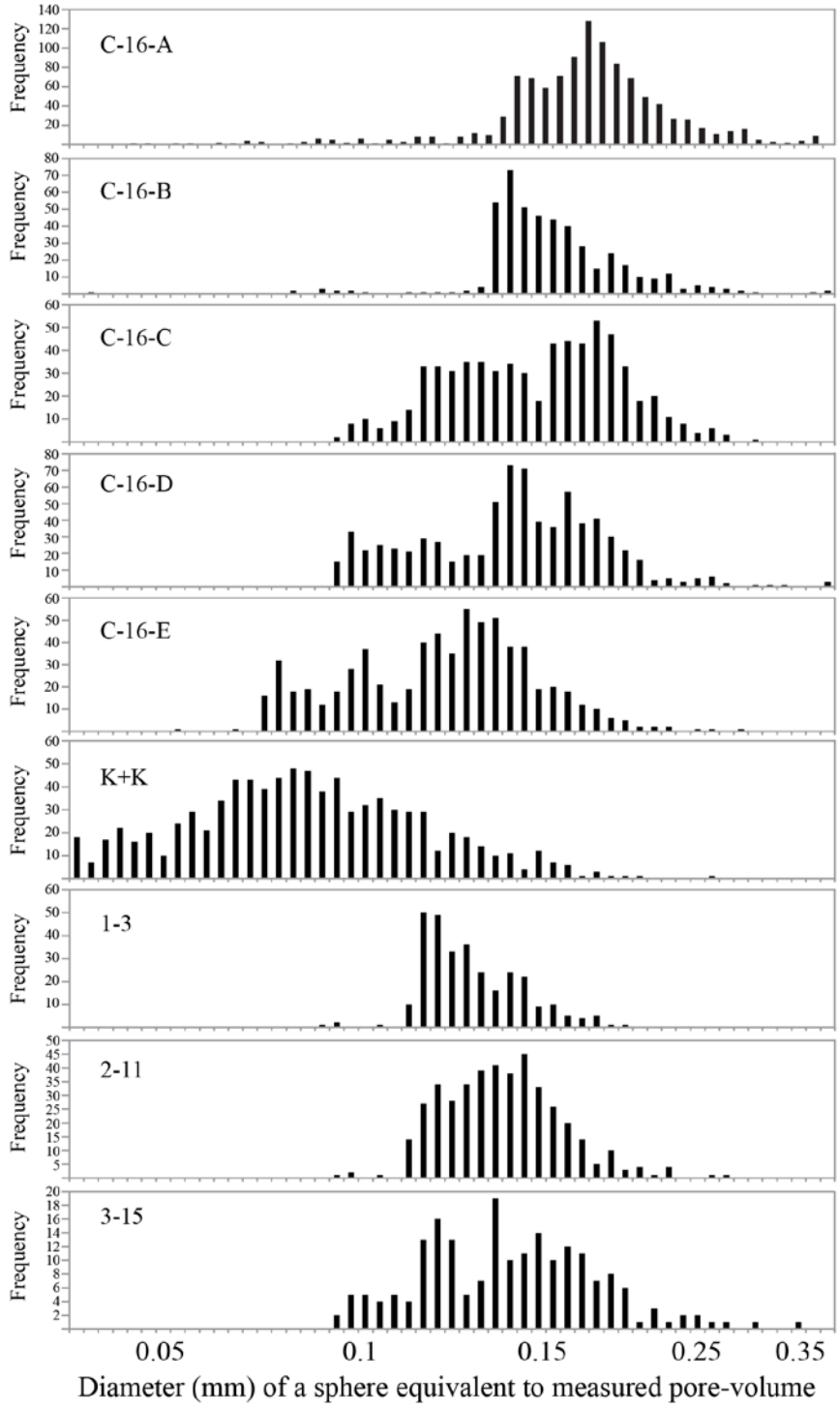

2.4.5 Pore Fabric Analysis

Despite the considerable diversity of pore sizes, distributions, and filling material in the carbonado sample set, all contain elongated pores with (apparent) preferred orientations. Nine samples were analyzed using Blob3D and all except C-16-C exhibit the same girdled long axes and clustered short axes of pores on a stereo-net (Figure 2.11). Stereo-nets are useful tools for compiling large amounts of 3-D data and projecting it in 2-D. Each dot on the stereo-net represents the appropriate axis (long or short) for each best-fit ellipsoid. The position of a dot corresponds to the trend and plunge of the axis. When a majority of the axes are oriented in the same plane, a girdled distribution arises; if the axes are pointing in the same direction, they form a clustered distribution. Stereo32 statistically analyzes the whole dataset and computes shape (K) and strength (C) parameters, which are suggestive of a foliation with a mild preferred orientation (Table 2.3; Figure 2.12). Furthermore, ellipsoid shapes were plotted on a ternary diagram using TriPlot (Graham and Midgley, 2000), which shows that 60% are compact-bladed to bladed to elongated. Comparable analysis of framesite diamond reveals similar fabric and pore shape (Figure 2.13).

The 3-D rose diagrams and fabric parameters from Quant3D analyses (Table 2.4) confirm the presence of an oriented pore fabric within all samples studied. However, the strength of pore orientation (DA [Degree of Anisotropy] parameter) varies among specimens. A DA value of 1 corresponds to an isotropic fabric while higher values correspond to more anisotropic fabrics. Three-dimensional (3D) rose diagrams for samples with lowest and highest DA parameters (3-18 and C-16-D, respectively) illustrate the range of pore-texture diversity among the carbonado specimens (Figure 2.14). Sample 3-18 has a preferred orientation of rod-like pores ($\tau1 > \tau2 \approx \tau3$), whereas sample C-16-D has slightly elongated platy pores in a preferred orientation ($\tau1 \approx \tau2 > \tau3$). Fabric strength and shape

measured using Quant3D vary, but most samples' pore fabrics are similar to the measured fabric from Blob3D analysis confirming a foliation with a mild preferred orientation ($\tau 1 > \tau 2 > \tau 3$). Table 2.4 also reports a BV/TV value which is a ratio of the volume of the material of interest to the total volume, which is effectively a measurement of porosity. Apparent porosity ranges from 4 % to 18 %, although some possibly large proportions of pores are omitted because they did not meet the threshold criteria. Thus, these represent minimum values for porosity.

Measured pore fabrics for both filled and unfilled varieties are similar, suggesting that the reason for this dichotomy is not associated with the cause of the fabric in carbonado. This also confirms that the measured pore-filling material fills or coats the shape of its precursor pores. If so, carbonado fabrics may be interpreted in terms of precursor pores formed during carbonado genesis rather than involvement of different secondary fabrics associated with mineral inclusions. This interpretation is supported by the similarity of pore shapes in sample C-16-C and 1-3 before and after acid leaching, when pore-filling material has been removed (Figure 2.15). Acid leaching also confirms that the carbonado pore network is connected in the samples tested. Exposure to concentrated HCl, HF, and HNO_3 for a total of 145 hours at > 90ºC removed a ~0.6 mm rind. While this is far from complete dissolution, a significant amount of material was still removed and demonstrates the diffusion-limited nature of acid dissolution in carbonado. Being able to image the interior before and after acid dissolution also sheds light on the nature of the material being removed. Florencite, a REE-rich aluminophosphate, is the most common mineral found within carbonado (Trued and De Wys, 1969, 1971) and likely to be the predominantly dissolved phase. Interestingly, isolated highly attenuating phases with a similar morphology to those found in the unfilled variety remained in 1-3 after leaching, revealing a phase that is more resistant to acid dissolution in the time given.

Figure 2.11 Pore Orientations

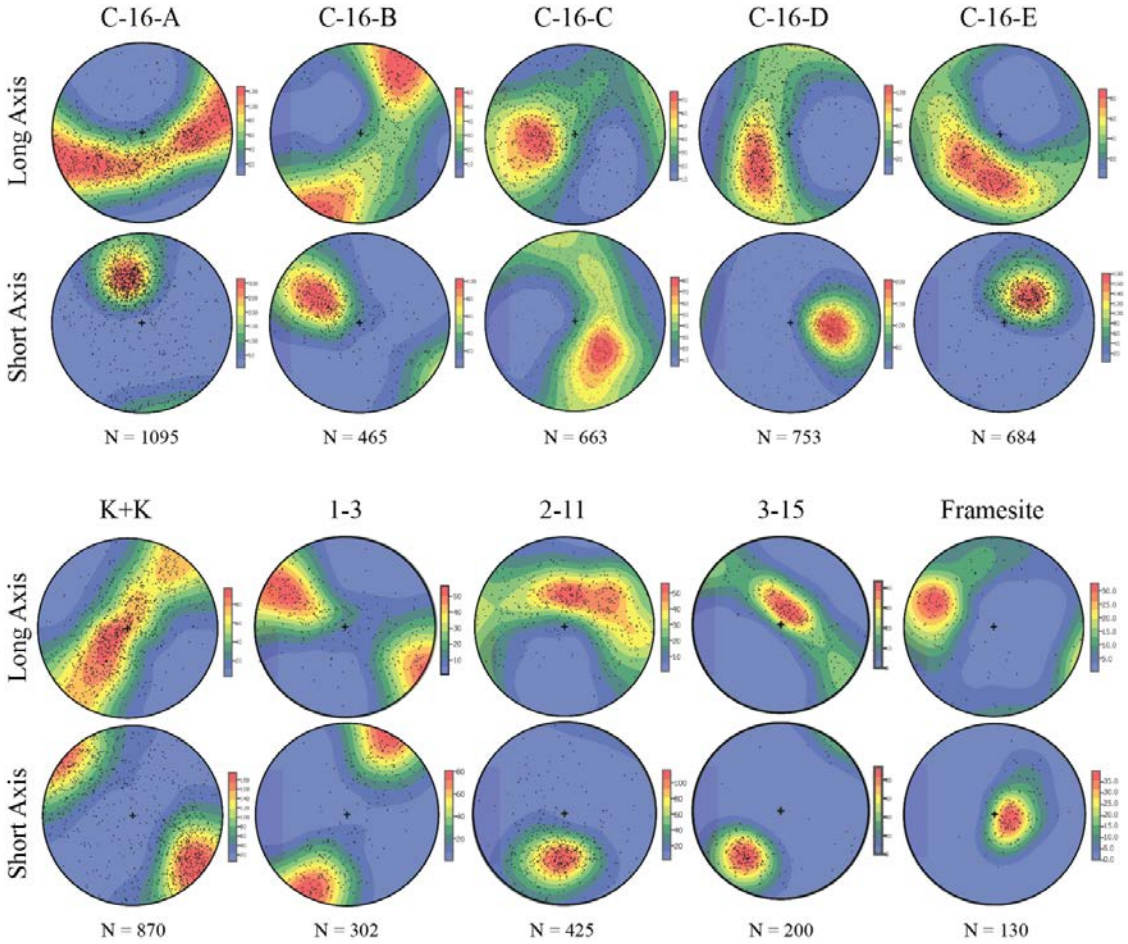

Pore best-fit ellipsoid orientations. N is the number of extracted objects per sample. Color bars show density contour values. Note a foliation fabric with a mild preferred orientation (slight clustering of long axes).

Figure 2.12 Fabric Strength and Shape for Blob3D Data

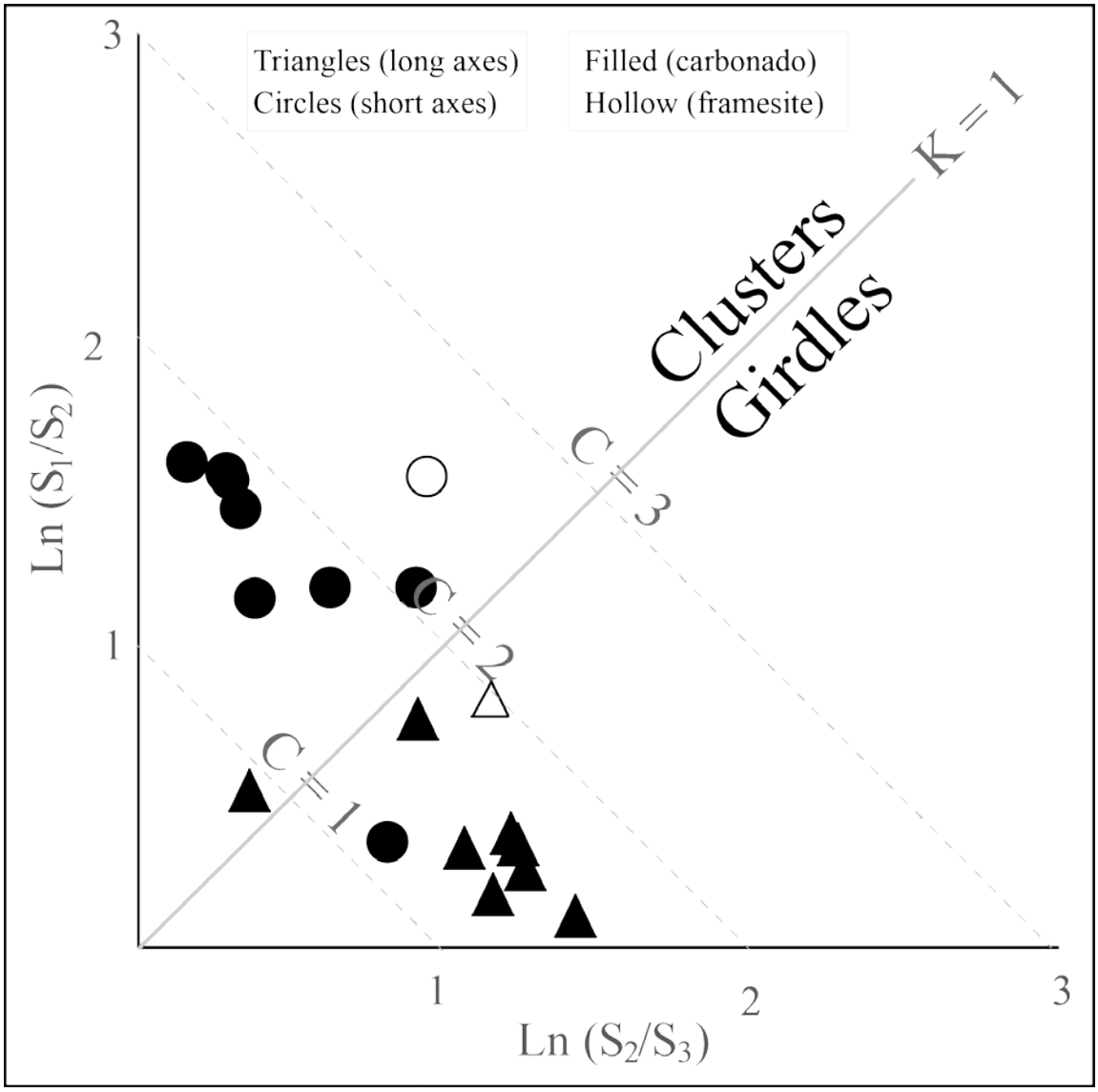

Eigenvalue ratio graph from Woodcock and Naylor (1983) for representing the shape (K) and strength (C) of samples. All samples except C-16-C have girdled long axes (K < 1) and clustered short axes (K > 1) with similar strengths (C). Higher strength values correspond to stronger and more organized fabrics.

Table 2.3 Fabric Parameters from Blob 3D Data

Sample	Axis	K	C	τ_1	τ_2	τ_3
C-16-A	Long	0.07	1.53	0.47	0.43	0.10
	Short	10.51	1.75	0.73	0.15	0.13
C-16-B	Long	0.31	1.39	0.51	0.37	0.13
	Short	1.93	1.81	0.68	0.21	0.11
C-16-C	Long	1.43	0.88	0.50	0.30	0.21
	Short	0.43	1.17	0.50	0.35	0.15
C-16-D	Long	0.38	1.59	0.53	0.36	0.11
	Short	5.18	1.84	0.73	0.16	0.12
C-16-E	Long	0.27	1.58	0.52	0.37	0.11
	Short	5.53	1.85	0.73	0.15	0.11
K+K	Long	0.15	1.33	0.48	0.40	0.13
	Short	3.04	1.53	0.65	0.21	0.14
1-3	Long	0.83	1.66	0.60	0.28	0.11
	Short	1.32	2.09	0.70	0.21	0.09
2-11	Long	0.21	1.53	0.50	0.39	0.11
	Short	4.31	1.79	0.71	0.17	0.12
3-15	Long	0.26	2.60	0.60	0.35	0.04
	Short	2.62	2.99	0.85	0.10	0.04
Framesite	Long	0.72	1.97	0.63	0.28	0.09
	Short	1.65	2.49	0.77	0.16	0.06

Shape (K) and strength (C) parameters and eigenvalues (τ_1, τ_2, τ_3) for short and long axes of measured pores calculated in Stereo32.

Figure 2.13 Pore Shapes

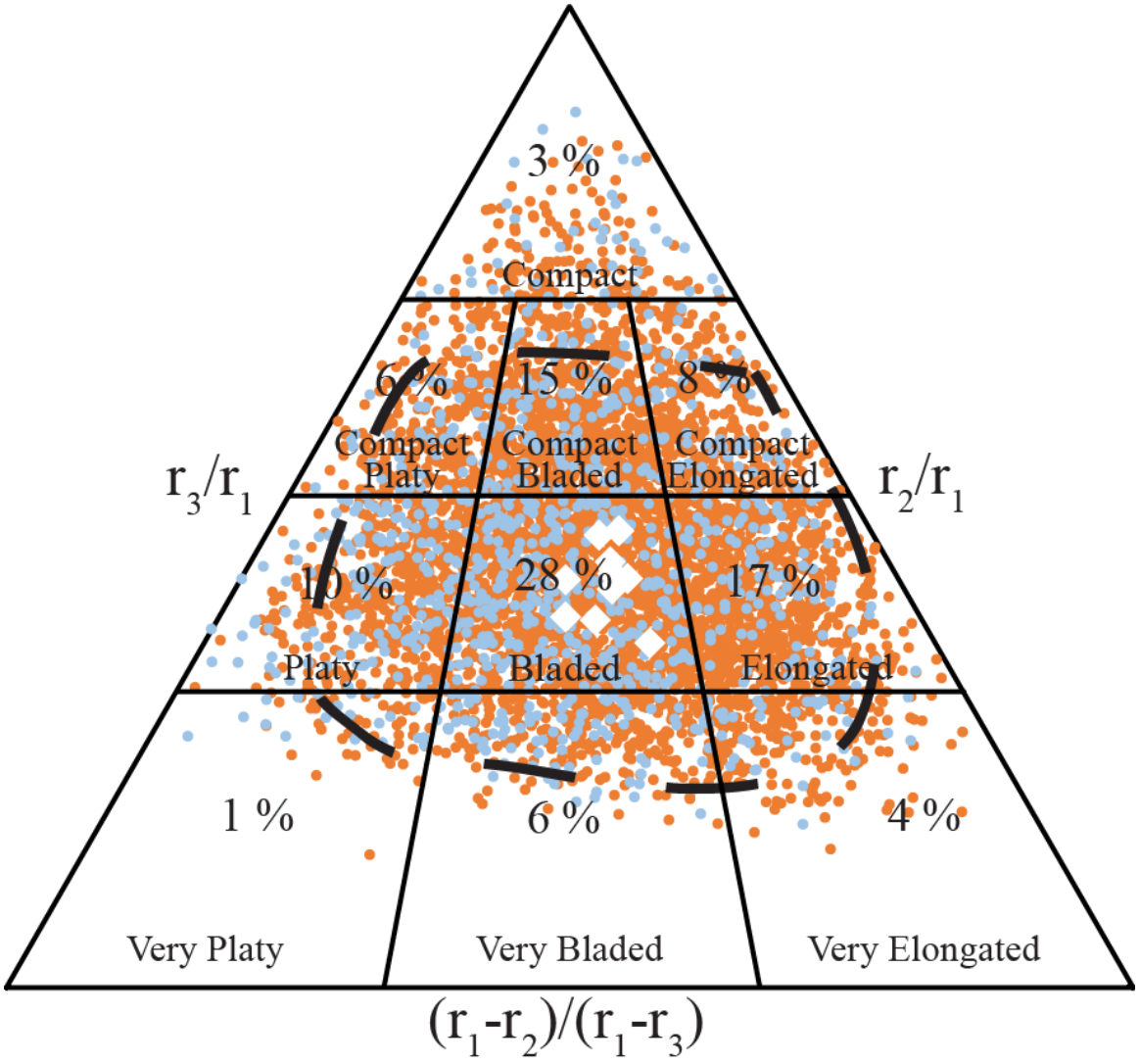

Pore best-fit ellipsoid shapes for all samples (N = 5,457). The "r" term in ternary axes denotes the long (r_1), intermediate (r_2), and short (r_3) axes of measured ellipsoid axes. Dashed line represents the area of framesite diamond data. African and Brazilian samples are represented by orange and blue dots, respectively. White diamond symbols represent the average of each carbonado sample. 60% of pores shapes fall within compact bladed to bladed to elongated classification fields.

Table 2.4 Quant3D Results

Parameters	C-16-A	C-16-B	C-16-C	C-16-D	M8348	N628	1-3	1-6	2-11	3-15 top	3-15 bottom	3-18
τ_1	0.51	0.48	0.47	0.46	0.44	0.44	0.48	0.41	0.44	0.43	0.47	0.44
τ_2	0.33	0.32	0.29	0.42	0.35	0.32	0.31	0.35	0.40	0.33	0.40	0.30
τ_3	0.16	0.20	0.24	0.12	0.21	0.25	0.20	0.24	0.16	0.24	0.13	0.26
DA	3.26	2.41	1.93	3.92	2.13	1.78	2.39	1.73	2.65	1.81	3.58	1.71
I	0.31	0.41	0.52	0.26	0.47	0.56	0.42	0.58	0.38	0.55	0.28	0.59
E	0.35	0.35	0.39	0.08	0.22	0.27	0.36	0.16	0.08	0.24	0.14	0.32
BV/TV	0.10	0.07	0.18	0.05	0.04	0.02	0.07	0.11	0.09	0.13	0.12	0.04

τ_1, τ_2, and τ_3 (1^{st}, 2^{nd}, and 3^{rd} eigenvalues, respectively) used to calculate other fabric quantities: DA (degree of anisotropy): τ_1/τ_3; I (isotropy index): τ_3/τ_1; E (elongation): $1 - \tau_2/\tau_1$. BV/TV (volume of material of interest/total volume)

Figure 2.14 3-D Rose Diagram from Quant3D Analysis

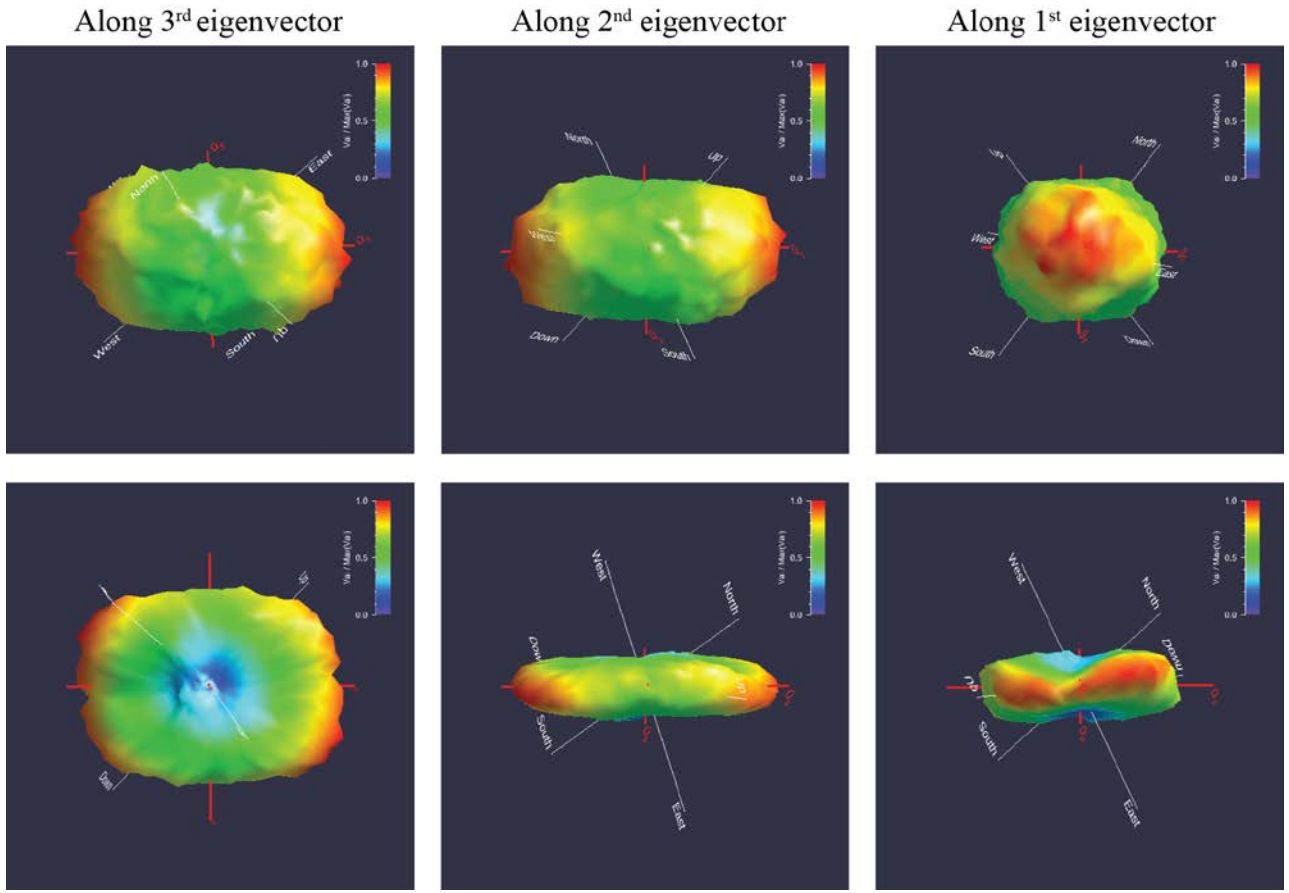

Three-dimensional (3D) rose diagram of pores for 3-18 (top; also see Fig. 2) and C-16-D (bottom; also see Fig. 3) viewing along the third, second, and first eigenvectors, showing preferred orientation. Colors and distance from the origin indicate relative strength of fabric according to the star volume distribution metric (Ketcham, 2005b)

Figure 2.15 XCT Images Before and After Acid Leaching

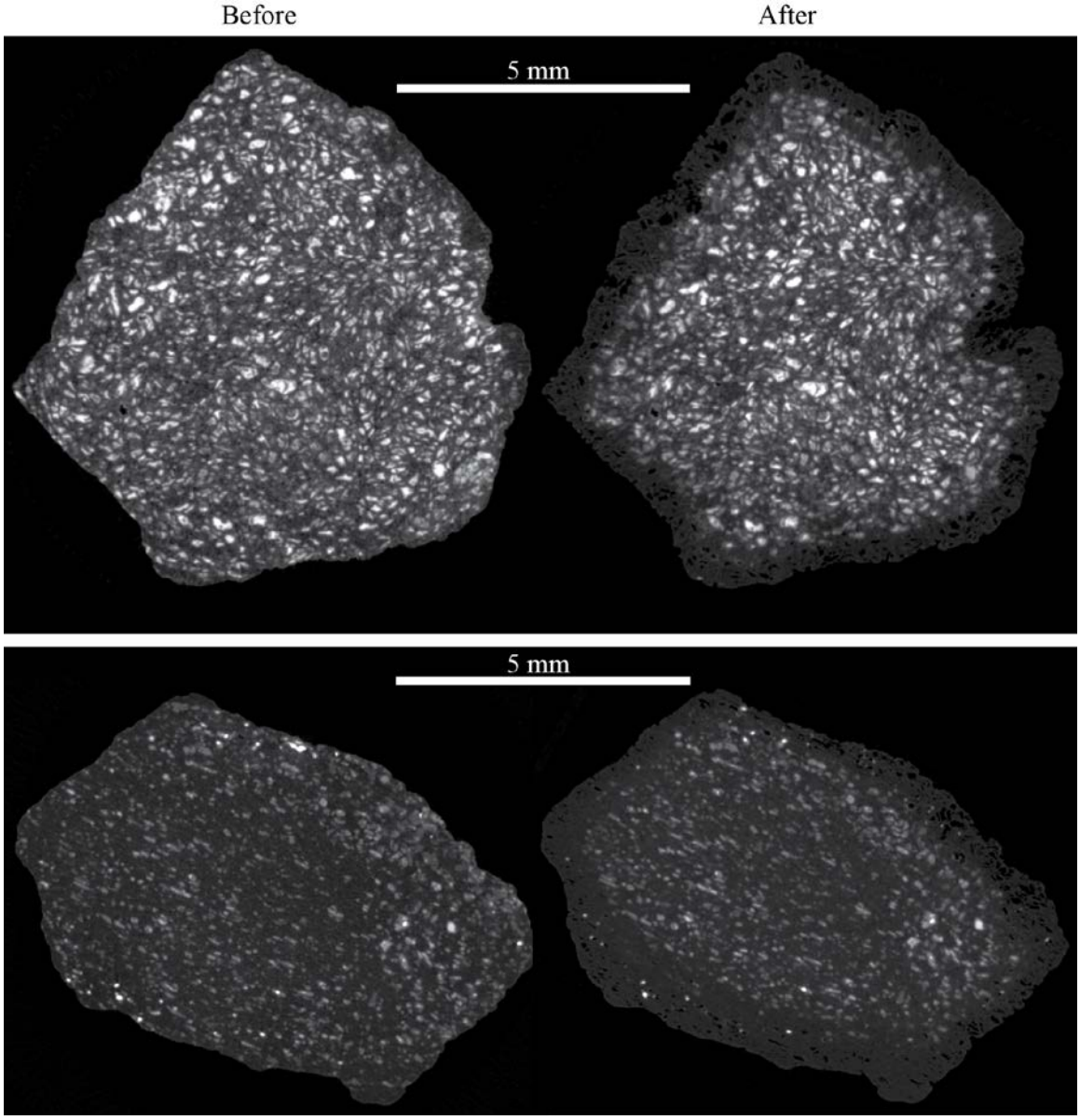

14.35-µm-resolution images encompassing entire specimens (C-16-C (top) and 1-3 (bottom)) before and after all acid leaching steps.

2.5 DISCUSSION

2.5.1 Implications from Textural Obsrvations

X-ray computed tomography reveals that carbonado specimens have diverse pore textures, with no systematic differences between African and Brazilian samples and, no pore texture that can be considered characteristic of carbonado. Despite this diversity, most samples have similar pore fabrics and shapes. Individual samples contain thousands to tens of thousands of pores (up to 18 % porosity), which vary in size from below the resolution of our XCT scans (2 µm/voxel) to greater than 1 mm in length (Figure 2.10).

We define three categories of carbonado based on their macro-inclusion suite: filled, intermediate, and unfilled (see figures 2.3, 2.4, and 2.5, above). Extending XCT imaging to the larger sample set of the present study confirms the observations of Ketcham and Koeberl (2013) that a polymineralic and disequilibrated composite is ubiquitous within carbonado pores of the filled variety, supporting the interpretation that the macro-inclusion suite within carbonado is secondary. Pervasive disequilibrium and alteration textures, evidence by diffuse boundaries, replacement textures, mottled morphologies among phases that evidently equilibrated at crustal P-T conditions supports that the pore network is almost fully 3-D connected and more mobile elements (*i.e.* uranium) may have been open to exchange with the surface.

The unfilled variety, however, includes material that is, at least in the XCT data, texturally different than the material in the filled variety. These isolated, more highly attenuating phases are apparently more homogeneous and nearly equant (Figure 2.4). Textures indicative of alteration and replacement, like those observed in the filled variety material, are not observed. This observation is consistent with this material being primary or forming by a process different from that generating the filled pore variety. Two scenarios

could explain their origin: (1) they are primary phases that have not been altered because these samples are less permeable and only areas near the edges of the grain have been infiltrated and altered to create the rim of less attenuating material (Figure 2.4); (2) the unfilled variety used to have the same secondary pore-filling material as the filled samples but subsequent dissolution from infiltrating fluids removed the more soluble phases and left behind the present inclusion suite. Some isolated highly attenuating phases remained after acid leaching (Figure 2.15), suggesting a more chemically resistant phase exists in carbonado, or some isolated pores exist and are not fully connected. Breakdown and alteration of these highly attenuating phases over time could conceivably have sourced the incompatible elements in the secondary minerals that evidently equilibrated at crustal PT conditions. In either case, the highly attenuating material within the unfilled variety may be the first unaltered primary macro-inclusion in carbonado.

The intermediate texture of C-16-D and N628 (see Figure 2.5, above) between the filled and unfilled varieties may also represent an environment for the formation of the present-day mineral assemblage similar to the conditions that led to the unfilled variety. The coherent 3-D volumes of material appear to be more compositionally similar, based on XCT grayscale values, than the heterogeneous composite of pore-filling material within the filled variety. Because volumes having sharp edges occur deep within samples, we postulate that these minerals formed from the spatially-limited *in situ* breakdown of primary phases, similar to the rim of less-attenuating material in the unfilled variety.

How these different textures of pore-filling material formed remains poorly understood. Ishibashi et al. (2016) suggested that contrasting crystal and pore size distributions and morphologies, UV-excited luminescence, and photoluminescence arose from variable exposure to annealing under thermodynamically stable P-T conditions. They categorize carbonado into A- and B-type where the latter were annealed leading to

coalescence or collapse of pores and reduced permeability. They also found no pore-filling material in their B-type sample, but they propose this could be a result of extensive polishing. Pore shape, size, and orientation are similar between the unfilled, intermediate, and filled samples suggesting that annealing was incomplete, leaving macro-pores that account for the distributions of filled and unfilled carbonado textures but collapsing micro-porosity to levels below the limits of detection of our XCT scans. Samples with pervasive low porosity regions may correspond to annealed B-type textures. Nevertheless, a difference in permeability among these filled, unfilled, and intermediate varieties seems most plausible for the differences in textures. In all carbonado samples, we were not able to identify continuous channels forming a connected network, indicating permeability connecting the larger pores observed in the XCT data exists along pores and grain boundaries below the resolution of our XCT data.

The euhedral cavity identified in C-16-D almost certainly represents a primary mineral that formed before or during carbonado crystallization and has since been lost (see Figure 2.6, above). This mineral would have formed coevally with, if not before, carbonado formation. Resorbed edges and diamond protruding into the cavity indicate this phase was not in chemical equilibrium with the diamond-forming media, and require that bulk carbonado crystallization had ceased before this phase had completely resorbed. The crystal habit of this cavity cannot be confidently identified, but orthorhombic, monoclinic, and triclinic minerals that are stable at diamond-forming conditions and are common inclusions within monocrystalline diamond (*e.g.* olivine, orthopyroxene, clinopyroxene, and rutile, among others). This mineral phase must have become unstable because an empty cavity with a thin lining of non-diamond material is all that remains. The lining material may preserve chemical components from the original phase not removed from the pore.

2.5.2 Implications from Pore Fabrics

Some authors have suggested that porosity in carbonado precludes a mantle origin (Garai et al., 2006; Haggerty, 2014), even though porous framesite diamonds are common in kimberlites. The porous structure of framesite is interpreted to indicate formation from carbon-rich fluids (Jacob et al., 2011) that were trapped during crystallization. Because diamond forms at > ~5 GPa, the confining forces would effectively eliminate any pore space in a crystallizing mass of diamond, so some phase(s) (fluids and/or minerals) had to be holding the pore spaces open. A similar process may be responsible for the pore network in carbonado, agreeing with recent hypotheses that carbonado formed in a fluid medium within the mantle (Ishibashi et al., 2012; Ketcham and Koeberl, 2013; Petrovsky et al., 2010). Extensive pores with irregular shapes are consistent with the proposition by Ketcham and Koeberl (2013) that the large pores represent globules of trapped fluid in a diamond crystal mush during the early formation of a proto-carbonado mass. We define the proto-carbonado mass as a loosely aggregated, fluid-rich crystalline mush that has not been completely crystallized containing the larger (10-250 μm), euhedral "phenocryst" diamonds and other primary crystalline phases, evidenced by the present-day euhedral cavities and pseudomorphs.

However, the preferred orientation and shape of pores needs explanation. This textural characteristic is ubiquitous throughout all studied carbonado samples and is certainly linked to their origin. Our measurements of pore fabrics are consistent with those of Ketcham and Koeberl (2013) and can be easily explained by their model where either the pores originally formed with this texture or a transient event deformed the proto-carbonado mass. The latter may be more likely as the observed pore fabric, a foliation with a mild preferred orientation, can arise from simple shear. Compaction, from an external force or through crystal settling would lead to a pure foliation and more tabular pores. On

the other hand, extension would create a lineation fabric with rod-like pores. A corollary to the simple-shear model is the presence of the pore-free planar zone observed in 3-15 and other samples that may be analogous to shear banding (see Figure 2.9, above). The heterogeneous distribution and density of pores may reflect deformation of a heterogeneous distribution of fluids in the proto-carbonado mass or from the mobilization of fluids.

A preferred orientation of pores caused by forces associated with simple shear may help explain the putative porphyrititc texture, as deformation might have provided the necessary pressure increase to drive the carbon-rich fluid well into the diamond stability field. This would lead to a drastic increase in nucleation rate and induce rapid crystallization of diamond to create the microdiamond "groundmass". By such a scenario, globules of trapped fluids were strained and frozen in place as the proto-carbonado mass became sintered together and diamond crystallization was driven to completion by the rapid increase in nucleation rate. The presence of deformation lamellae and high residual stress in the microdiamond population can be attributed to this deformation event. Additionally, this event may have created fractures and fissures in the proto-carbonado mass, providing a location and mechanism for the formation of columnar diamond (Rondeau et al., 2008) as well as the healed fractures we observe here.

This transient increase in pressure may be associated with a rapid drop in oxygen fugacity that would enhance rapid diamond crystallization and explain the occurrence of highly reduced phases only located in microdiamond populations (Sautter et al., 2011). The observed SiC, TiN, and native Ti mineral assemblage requires an oxygen fugacity of ~IW -15, which, they claim, can only be achieved by percolation of ultra-reduced H_2-CH_4 fluids through the proto-carbonado mass. However, the source of such highly-reduced fluids is not known. Ishibashi et al. (2012) claim an oxygen fugacity only around FMQ -3 is necessary to explain their observed reduced inclusion suite, which are more reasonable

conditions for the mantle. Nevertheless, a transient event led to a rapid decrease in the oxygen fugacity and likely drove the carbon-rich fluids away from equilibrium. The stage-1 diamond “phenocrysts” indicate growth in optimal conditions, while the stage-2 microdiamond groundmass indicates a rapid increase in the number of nucleation sites, leading to pervasive diamond crystallization.

Our observations reasonably accommodate those of Sautter et al. (2012) that deformation may be coeval with a reduction in oxygen fugacity. However, they claim the proto-carbonado mass was completely solidified and solid-state deformation led to granulation of some of the larger diamonds to create the porphyritic texture. Solid-state deformation would not preserve euhedral non-diamond phases like those documented in this study and Ketcham and Koeberl (2013); the preservation of euhedral, non-diamond phases can only be explained by deformation of a loosely aggregated mass. Final crystallization and deformation likely occurred shortly before or during ascent to the crust, as the microdiamond population contains unaggregated nitrogen suggestive of very short residence in the mantle. A “redox-freezing of a loosely aggregated diamond mass” model bears similarities to the model proposed by Jacob et al. (2011) that framesite crystallized rapidly through a small-scale redox reaction between C-O-H-rich fluids and reduced sulfide-bearing eclogite, though the extent and cause of reduction vary between the two models. Thus, the rapid reduction of an oxidized carbon supersaturated fluid, in addition to the pressure increase associated with deformation, provides ample driving forces for inducing pervasive diamond crystallization.

Chapter 3: Inclusion Trace Element Geochemistry

3.1 INTRODUCTION

For as long as carbonado has been studied, it has been recognized that the pore network is filled/lined with minerals that evidently equilibrated at crustal P-T conditions (Trued and De Wys, 1969, 1971). Among the identified phases, florencite, which can host 10's of wt. % rare earth elements, is the dominant mineral, and commonly forms from the hydrothermal alteration of monazite. It has been reported as fracture-filling disconnected from external surfaces in a monocrystalline diamond from Kankan, Guinea (Brenker et al., 2008), and interpreted as having formed from decompression and devolatilization of a trapped fluid inclusion during entrainment and ascent in a kimberlite. Regardless of its origin, florencite is unstable at diamond-forming conditions and likely occurs as a secondary mineral. Its high REE content and occurrence in carbonado thus requires an explanation. Few studies have attempted measuring the REE concentrations in this suite of crustal minerals and none have provided a complete trace element dataset. We have measured, for the first time, the concentrations of the entire trace element suite and are able to evaluate the effectiveness of acid leaching procedures on carbonado.

3.2 METHODS

3.2.1 Analysis on Exterior Minerals

During the study by Ketcham and Koeberl (2013), the sample was cut in half using a laser to expose one of the rhombic dodecahedral pseudomorphs in the interior. We examined the exterior surface of this sample using a Phillips/FEI XL 30 ESEM in low-vacuum mode to image and identify elements comprising highly attenuating phases identified in the XCT volume. Two zircon crystals lodged in exterior pores were identified

and subsequently analyzed for U-Pb geochronology using an Element 2 HR-ICP-MS equipped with an Excimer laser at the University of Texas at Austin UTChron Labs (Figure 3.1).

Figure 3.1 Zircon in Exterior Pores

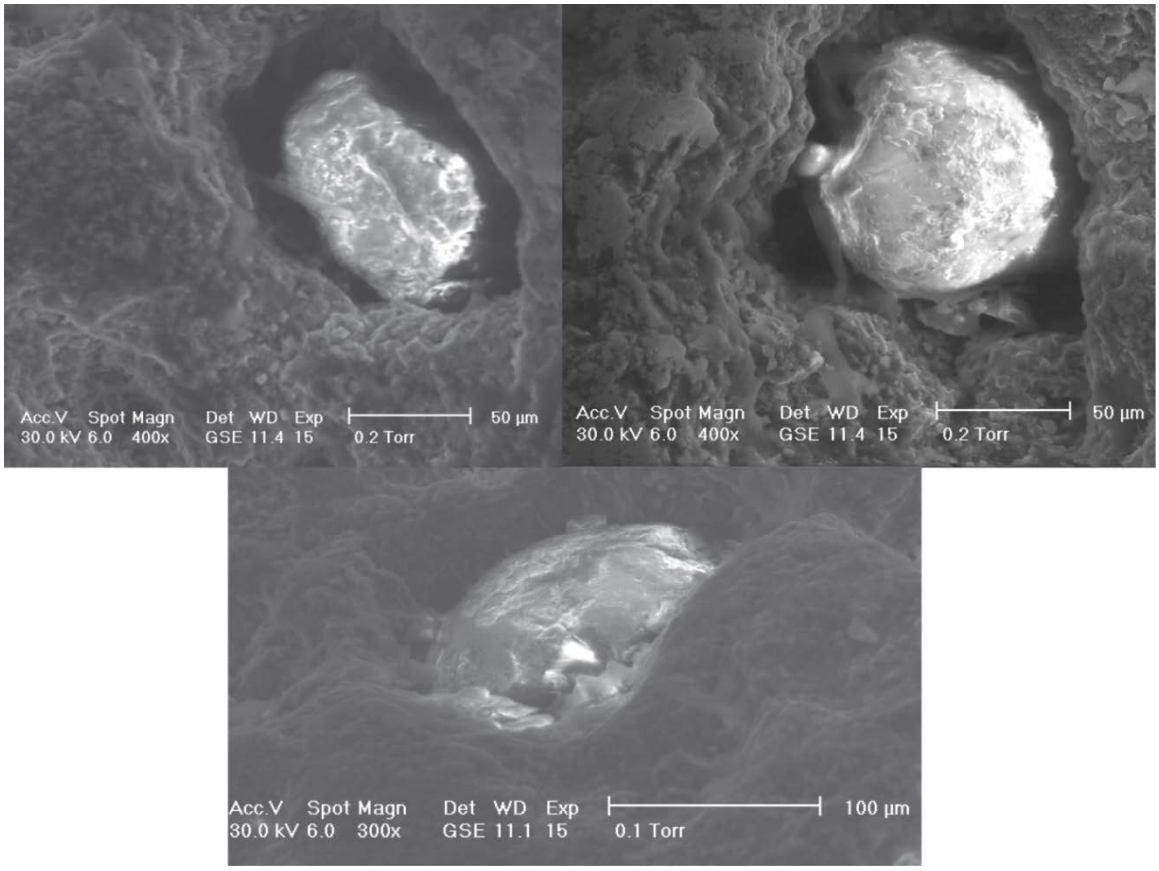

Secondary electron images of K+K (top) and 3-17 (bottom) showing zircon crystals lodge in exterior pores.

3.2.2 Acid Leaching Procedures

After imaging the textures of pore-filling materials, three African (C-16-A, C-16-C, and C-16-E) and two Brazilian samples (1-3 and 3-16) were selected to determine the trace element (REE's and incompatible elements) composition of pore-filling material dissolved in successive and combined leaching steps (HCl wash, HF:HNO_3 leach, aqua

regia leach). All steps were performed in sealed 15 mL Savillex™ beakers with screw tops using optima-grade 12 M HCl, optima-grade concentrated HF, and doubly-distilled 15.6 M HNO_3. Initial sample masses were measured using a microbalance with 1 µg precision. In an effort to remove any surface contamination, samples were reacted twice in 6 N HCl at 90˚C for 1 hour in sealed containers and the leachate saved for analysis. Samples were then ultrasonically rinsed in their original containers (twice) in ultrapure 18.2 megaohm water for 30 minutes, and the water was combined with the original HCl leachate for analysis. After surface cleaning, the samples were dried for 72 hours on a hot plate at 140˚C and masses reweighed. Next, samples were submerged in 4-6 mL of 4:1 HF:HNO_3 at 140˚C for 72 hours in sealed beakers. The HF:HNO_3 leachate was saved and the samples were ultrasonically rinsed in ultrapure water for 30 minutes. The water was combined with the HF:HNO_3 leachate and saved for analysis. Again, the samples were dried for 72 hours at 140˚C on a hot plate and masses determined. Finally, samples were submerged in 4-6 mL of aqua regia (2:1 HNO_3:HCl) at 140˚C for 72 hours in sealed containers. The aqua regia leachate was saved, the sample washed in ultrapure water, and the leachate and wash water combined and saved for analysis. Final sample masses were measured after drying for 72 hours at 140 ˚C. Samples C-16-C and 1-3 were rescanned using the same XCT parameters to assess the effectiveness of acid leaching. All leachates were evaporated to dryness on a hot plate at 110˚C, re-dissolved in 1 mL of 1 N HNO_3, and transferred in acid-cleaned 1.5 mL microcentrifuge tubes for subsequent dilution and ICP-MS analysis. All sample preparation was performed in the Radiogenic Isotope Clean Lab at the University of Texas at Austin.

Incompatible element and REE concentrations were measured using an Agilent 7500ce ICP-MS at the University of Texas at Austin. Aliquots of the 1 mL sample leachate solutions (and procedural blanks) were initially diluted 500-fold in 2% v/v HNO_3 and

analyzed using a semi-quantitative method to provide rough estimates of elemental concentrations. Using these values, solutions were further diluted to obtain La concentrations close to 50 ppb. For quantitative analyses, the instrument was optimized for sensitivity in "no gas" mode and low oxide production (CeO/Ce 1.05 ± 0.05%) (Table 3.2). Argon nebulizer and make-up gas flow-rates were 0.95 and 0.25 L/min, respectively. Pulse/analog normalization factors were determined to ensure that pulse and analog detection modes of the electron multiplier provided comparable sensitivities for samples with a wide range of concentrations. The instrument was then tuned in He-mode, with an optimized flow-rate of 5.5 mL/min for kinetic energy discrimination. An internal standard solution (Ga, In, Re at 500 ppb), consistently added to the unknown via peristaltic pumping, was used to compensate analytes for instrumental drift. All analytes except K were measured in no-gas mode. Blanks (2% HNO_3) were measured in replicate (n=2) following the calibration sequence, and interspersed with a quality control standard within the unknown sequence.

Calibration standards were prepared from certified multi-element stock reference standard solutions (Inorganic Ventures and VHG Labs). Calibration standards for REE's, Y, Nb, Hf, and Ta were targeted for 100, 10, 1, 0.1, 0.01, 0.001, and 0 ppb. Standards for Rb, Zr, Cs, Ba, Pb, Th, U were made at concentrations of 1000, 100, 10, 1, 0.1, 0.01, and 0 ppb. Standards for K were made at concentrations of 6250, 625, 62.5, 6.25, 0.625, 0.0625, and 0 ppb. Standards for Sr were made at concentrations of 5000, 500, 50, 5, 0.5, 0.05, and 0 ppb. All calibration curves were highly linear, with correlation coefficients (rho) $\geq$ 0.999. Single-element Ba and LREE (Ce, Pr, Nd, Sm, Eu, Gd, and Tb) standards (200 ppb) made from certified reference standards (Inorganic Ventures™ and Assurance™), were used to measure the production ratio of Ba- and select LREE-oxide/hydroxide species that interfere particularly with middle and heavy REEs. Analyte selection and methodology for oxide

correction were based on least interfered species with the highest natural abundances, (following standardized approaches (Aries et al., 2000; Dulski, 1994; Négrel et al., 2006)). Oxide production ratios (MO^+/M^+ and MOH^+/M^+) were measured for each single element standard and oxide overlap intensity was subtracted from the interfered analyte intensity. Background and drift corrections were applied to raw intensities before compensation for oxide/hydroxide overlaps. Final correction intensities were then used to establish the linear intensity-concentration regressions used for quantification. Limits of detection were < 1 ppb, except K at < 4 ppb. Procedural blanks were all below detection. Analyte recoveries for a 10 ppb quality control standard (made from certified stocks independent of the calibration standards) were within 6%, except K was 22%. Leachate concentrations for most analytes exceeded detection limits by factors of 10-1000 (Table 3.1).

Table 3.1 Instrumental detection limits, signal to noise ratios, and analyte recoveries

			Average Concentration in leachate fraction (ppb)			Signal to Noise Ratio			Quality Control (N=3)		
Element	Isotope Measured	Limits of Detection (ppb)	HCl	HF:HNO_3	Aqua Regia	HCl	HF:HNO_3	Aqua Regia	Concentration (ppb)	Measured (ppb)	Recovery
K	39	3.426	1651.94	6.41	2.37	482.1	1.9	0.7	10.10	12.32	1.22
Rb	85	0.026	3.68	0.02	0.02	140.5	0.9	0.8	10.18	10.30	1.01
Sr	88	0.097	12.19	18.18	39.76	125.7	187.4	409.9	50.90	50.90	1.00
Y	89	0.004	12.17	2.56	4.49	3109.6	655.3	1148.3	9.96	9.70	0.97
Zr	90	0.066	14.38	55.28	0.13	219.3	843.1	1.9	20.30	19.12	0.94
Nb	93	0.004	0.28	0.34	0.00	77.6	93.3	0.2	10.12	9.52	0.94
Cs	133	0.023	0.31	0.00	0.00	13.9	0.1	0.0	10.18	10.32	1.01
Ba	137	0.027	57.11	17.42	23.86	2134.7	651.2	892.0	10.18	10.16	1.00
La	139	0.019	23.14	14.08	41.23	1245.8	758.1	2219.9	9.96	9.89	0.99
Ce	140	0.026	46.21	49.62	57.90	1774.0	1905.1	2223.0	9.96	9.80	0.98
Pr	141	0.004	4.35	2.61	6.47	1205.8	725.3	1795.2	9.96	10.10	1.01
Nd	146	0.011	14.79	9.13	20.01	1295.3	799.4	1753.0	9.96	9.47	0.95
Sm	147	0.002	3.00	1.72	3.04	1255.6	721.2	1274.5	9.96	9.80	0.98
Eu	151	0.002	0.67	0.34	0.61	356.6	181.9	324.7	9.96	10.30	1.03
Gd	157	0.003	2.90	1.42	2.54	1061.5	520.4	929.3	9.96	9.80	0.98
Tb	159	0.014	0.42	0.15	0.30	30.2	10.7	21.2	9.96	10.18	1.02
Dy	163	0.003	2.30	0.65	1.33	880.4	247.7	509.0	9.96	9.88	0.99
Ho	165	0.002	0.46	0.12	0.23	215.6	54.5	106.8	9.96	10.29	1.03
Er	167	0.002	1.22	0.31	0.55	551.6	139.0	250.3	9.96	9.82	0.99
Tm	169	0.002	0.17	0.04	0.07	75.0	19.5	32.6	9.96	10.21	1.02
Yb	172	0.002	1.02	0.28	0.47	515.2	140.6	237.7	9.96	10.07	1.01
Lu	175	0.003	0.14	0.04	0.06	41.8	11.8	19.5	9.96	10.08	1.01
Hf	178	0.011	0.42	1.16	0.01	39.2	107.7	1.0	10.12	9.18	0.91
Ta	181	0.007	0.00	0.02	0.00	0.6	3.2	0.2	10.12	9.67	0.96
Pb	208	0.032	99.38	18.36	31.53	3120.6	576.5	990.0	10.18	10.75	1.06
Th	232	0.128	8.57	2.10	2.24	66.8	16.4	17.4	20.14	20.55	1.02
U	238	0.034	4.61	0.84	0.03	135.2	24.8	0.8	20.14	20.80	1.03

Table 3.2 Agilent 7500ce ICP-MS operating conditions

Instrumental Parameter	Value/Notes
Nebulizer	PFA microflow concentric (quartz glass)
Spray chamber	Peltier-cooled Scott-type (quartz glass)
Spray chamber temperature	2°C
Carrier gas flow rate	0.95 L/min
Makeup gas flow rate	0.25 L/min
Nebulizer pump speed	0.1 rps
RF power	1600 W
Torch sample depth	8 mm
Acquisition mode	Spectrum analysis (Multi-tune)
Integration time per point	0.1 sec
Number of points per mass	3
Integration time per mass	0.3 sec
Sampling period	0.82 sec
Total acquisition time	94.04 sec

3.3 RESULTS

3.3.1 Zircon in Exterior Pores

U-Pb geochronology analysis of sample K+K zircon crystals yielded ages of 573.2 ± 4.3 Ma on 4 spot-analyses and 901 Ma on 2 spot-analyses with large uncertainties (Figure 3.2). The younger age may correspond to magmatism associated with the Pan-African orogeny and the older age with the breakup of Rodinia. These ages depart greatly from the reported minimum and maximum possible ages of carbonado (2.6 to 3.8 Ga), suggesting they are likely detrital zircons that became lodged in external pores or possibly introduced anthropogenically during mining/preparation.

Figure 3.2 Zircon Ages

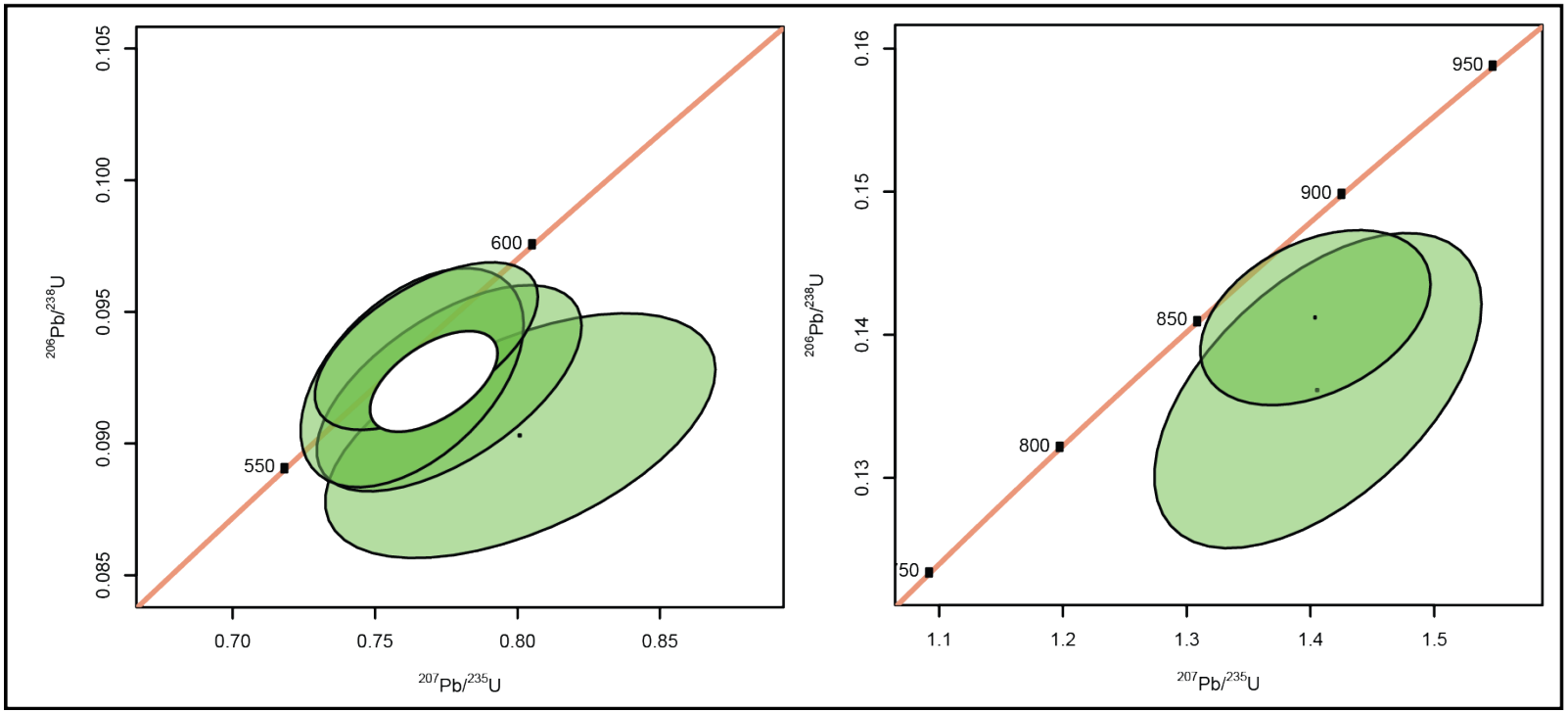

Concordia diagrams for the two analyzed zircons. Reported ages are 573.2 Ma ± 4.3 Ma and 901 Ma with large uncertainties.

3.3.2 REE and Trace Element Concentrations

Table 3.3 reports REE and trace element concentrations as well as separate and combined mass losses of material removed from carbonado pore networks in strong acid leaching (HCl, HF:HNO_3, and aqua regia. Concentrations for K and Cs in most aqua regia leachates were below the limits of detection (3.4 ppb and 0.02 ppb, respectively). Elemental data for the HF:HNO_3 leachates are only reported for sample C-16-E because insoluble fluorides in the other sample during HF evaporation. Several attempts to dissolve these precipitates by serial dilution in 1N HNO_3, 6N HNO_3, aqua regia, and perchloric acid proved unsuccessful. The initial HCl leachates likely represent a mixture of crustal contamination and some internal material, so are not used for interpretations. The intermediate HF and final aqua regia leachates, which are substantially richer in REE and incompatible-elements, provide the main basis for interpreting the composition of material within carbonado pore networks.

Rare earth element-bearing phases were dissolved to variable degrees by the different acids in the order of aqua regia > HF:HNO_3 > HCl. Total REE (ΣREE) concentrations in the HCl leachates (90 to 611 ppm) are negligible compared to those in the aqua regia leachates (95,730 ppm to 419,340 ppm), with the HF leachate having an intermediate concentration (3,680 ppm). All leachates are dominated by LREE enrichments with Ce as the dominant element followed by La and Nd. Among the aqua regia leachates, the ΣREE for C-16-A are ~40 % higher than the next most concentrated samples, C-16-C and 3-15, which in turn are ~45 % and 61% greater than samples 1-3 and C-16-E, respectively. Sample C-16-E, which has the lowest ΣREE concentration among aqua regia leachates, is still more than 25 times its HF:HNO3 counterpart. Thus, aqua regia may preferentially dissolve REE-rich phases. The combined concentration in the material

removed from C-16-E for HF:HNO3 and aqua regia leachates is also reported in Table 3.3. The C-16-E combined value reasonably approximates modal compositions of the leachable inclusion material.

The amount of uranium, thorium, and lead is variable among the leachates with most having high Pb concentrations and lower U. Uranium is strongly depleted compared to thorium in the aqua regia leachates, with average Th/U = 115 and average U concentration at 47 ppm. The average Th/U when U concentration is < 47 ppm is 139 while Th/U at higher U concentration (> 47 ppm) is 18. The HCl leachates have more variable Th/U (0.2-8.2), but have lower average U concentrations on average (17 ppm). The HF:HNO_3 leachate has 35.2 ppm U and a Th/U of 2.5. In all leachates, Pb is enriched compared to Th, with the highest Pb concentration in 3-16 (aqua regia) at 98,961 ppm (9.9 wt. %). The C-16-E combined values has Th/U of 17, uranium concentration of 29.7 ppm, and 2214 ppm Pb.

The REE concentration of the leachates normalized to CI chondrite (McDonough and Sun, 1995), figure 3.3, shows the distinct overall REE enrichment in the aqua regia and HF:HNO_3 compared to the HCl leachates. All samples have nearly linear patterns with LREE enrichments and slight negative Eu anomalies with an average Eu/Eu* at 0.75. ($Eu/Eu^* = Eu_N/[(Sm_N)(Gd_N)]^{1/2}$, where N denotes chondrite normalized values (McLennen et al. 1990)). Slight positive Ce anomalies exist in sample C-16-E (HCl and HF:HNO_3) (Ce/Ce* 1.45 and 2.03, respectively) ($Ce/Ce^* = Ce_N/[Ce_N^2/Nd_N]$, where N denotes chondrite normalized values (Lawrence et al., 2006)). Less pronounced negative Ce anomalies exist in samples C-16-C and 1-3 (Ce/Ce* = 0.76 and 0.69, respectively). Trace element concentrations normalized to CI chondrite (McDonough and Sun, 1995), figure 3.4, illustrate similar patterns among the aqua regia leachates but at different concentrations. High field strength elements (Zr, Nb, Hf, and Ta) and Cs, Rb, and K are

depleted up to ~ 6 orders of magnitude within aqua regia leachates. Sample C-16-E ($HF:HNO_3$) shows a similar trend except for Zr and Hf. C-16-E combined displays a similar trend to the aqua regia leachates, but with less pronounced Zr and Hf depletions.

Table 3.3 Trace Element Concentrations in Carbonado Pore-Filling Material

Element, (ppm)	HCl					HF	Aqua Regia					Combined
	C-16-A	C-16-C	C-16-E	1-3	3-16	C-16-E	C-16-A	C-16-C	C-16-E	1-3	3-16	C-16-E
K	5181	3385	2091	8461	10863	267	679	-	-	14879	-	211.2
Rb	17.99	9.96	5.30	14.46	13.77	1.02	2.78	1.65	0.26	94.87	3.58	0.86
Sr	22.94	72.59	5.17	55.24	87.75	757.5	199567	95325	15167	19647	24453	3769
Y	15.86	20.80	9.91	189.09	25.69	106.83	10386	5852	4041	7557	1722	928.9
Zr	62.81	31.57	21.91	62.20	64.56	2303	16.29	8.78	201.16	105.58	422.67	1864
Nb	0.40	1.33	0.42	1.21	1.75	14.17	1.61	0.62	0.12	0.20	3.91	11.23
Cs	2.54	0.29	0.57	0.56	0.56	0.07	-	-	-	5.70	-	0.059
Ba	143.1	449.7	32.08	225.0	301.7	798.6	75030	61786	16189	20653	30097	4015
La	94.02	117.58	12.91	123.0	118.1	648.7	140847	90849	22896	39963	71674	5298
Ce	153.1	224.6	41.40	263.6	234.1	2285	176267	100460	44079	53363	125468	11019
Pr	14.81	18.39	3.64	29.19	21.65	120.4	18478	11613	4648	7792	11715	1066
Nd	48.38	58.58	15.09	102.14	69.57	419.9	57140	33194	16119	25384	32153	3700
Sm	10.46	9.63	4.20	17.72	10.38	75.12	9183	4090	2862	3508	3223	657.4
Eu	2.32	1.97	0.96	4.33	2.19	14.98	2046	833.7	581.2	684.8	517.5	133.3
Gd	7.98	7.20	3.63	18.01	9.25	47.99	6897	2636	1961	2267	1337	447.8
Tb	1.27	1.00	0.63	2.89	1.29	5.90	969.1	370.9	241.1	324.0	159.9	55.05
Dy	6.75	5.22	3.58	19.07	6.42	28.09	4435	1948	1136	1749	683.0	259.6
Ho	1.17	0.93	0.63	4.72	1.19	5.06	666.9	353.7	196.1	334.6	99.25	44.98
Er	2.96	2.33	1.63	13.29	2.87	13.32	1327	745.8	494.2	972.4	219.5	113.8
Tm	0.44	0.32	0.24	1.78	0.42	1.94	153.91	74.07	66.57	160.1	28.19	15.45
Yb	2.89	2.05	1.52	9.68	2.34	11.93	824.42	360.8	398.1	1139	169.9	92.6
Lu	0.39	0.29	0.20	1.27	0.36	1.67	105.9	39.50	53.72	166.4	21.79	12.5
Hf	2.08	0.74	0.72	1.57	1.72	48.25	20.64	9.88	11.11	8.26	32.67	40.49
Ta	0.01	0.01	0.00	0.02	0.04	1.00	4.01	2.07	1.12	1.75	2.78	1.02
Pb	563.1	80.75	65.15	268.7	817.5	765.0	61212	61713	7700	29560	98961	2214
Th	69.70	10.91	12.14	20.27	17.37	87.41	2441	1709	2052	5122	1814	497.9
U	8.50	46.76	4.49	5.87	17.07	35.20	138.7	11.70	8.80	45.34	28.17	29.68
∑ REE	347	450	90	611	480	3680	419340	247569	95731	137807	247469	22916
$(La/Lu)_N$	25	42	7	10	34	40	138	239	44	25	341	44
Eu/Eu*	0.78	0.72	0.75	0.74	0.68	0.76	0.78	0.77	0.75	0.74	0.76	0.75
Ce/Ce*	1.04	1.20	1.45	0.97	1.07	2.03	0.91	0.76	1.01	0.69	0.90	1.10
Mass Loss (µg)	8799	3638	5939	1997	2305	36487	11211	18198	9639	6663	5211	46126

Figure 3.3 Carbonado REE Patterns

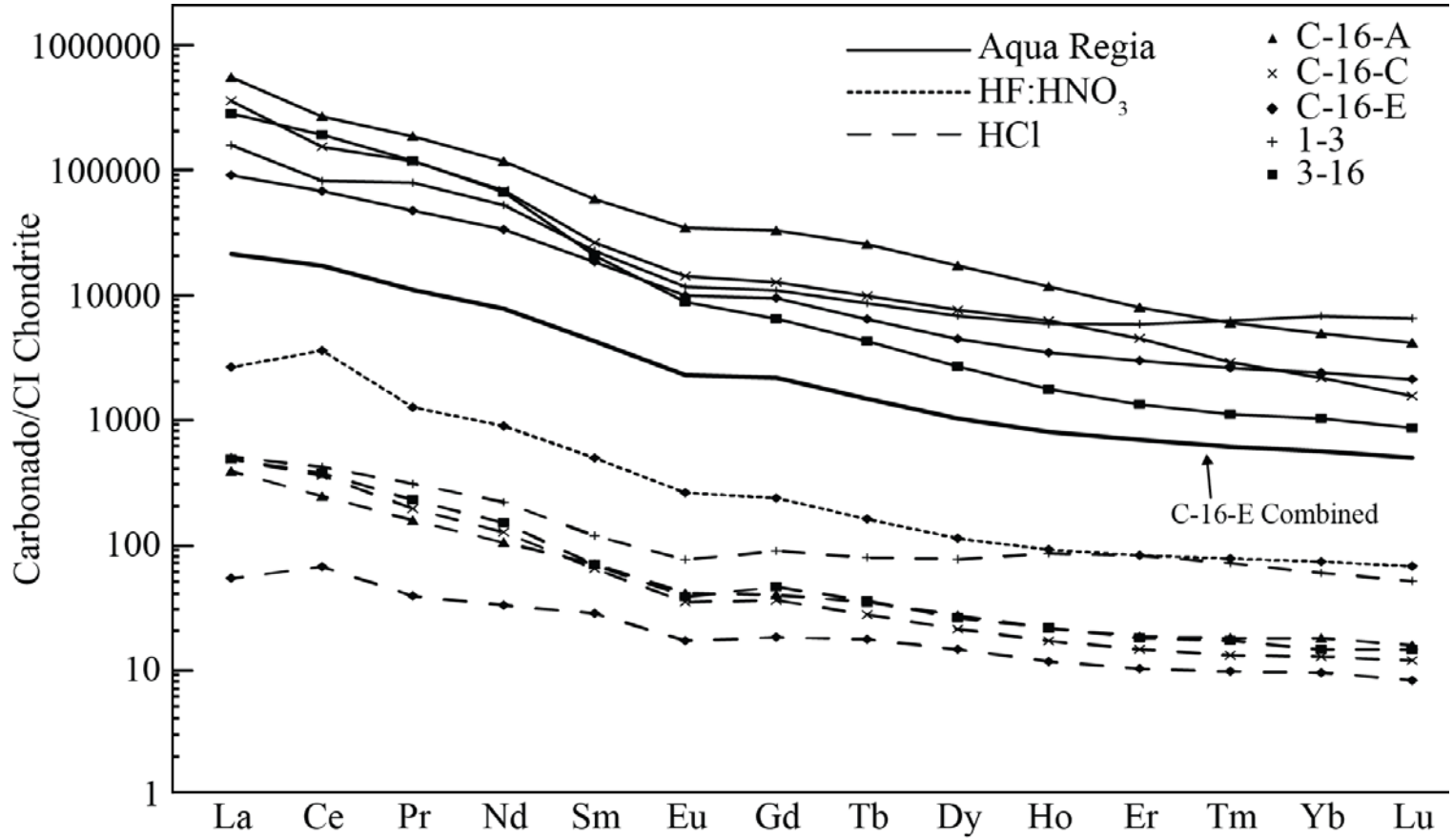

CI Chondrite (McDonough and Sun 1995) normalized REE patterns of all analyzed leachates.

Figure 3.4 Carbonado Trace Element Pattern

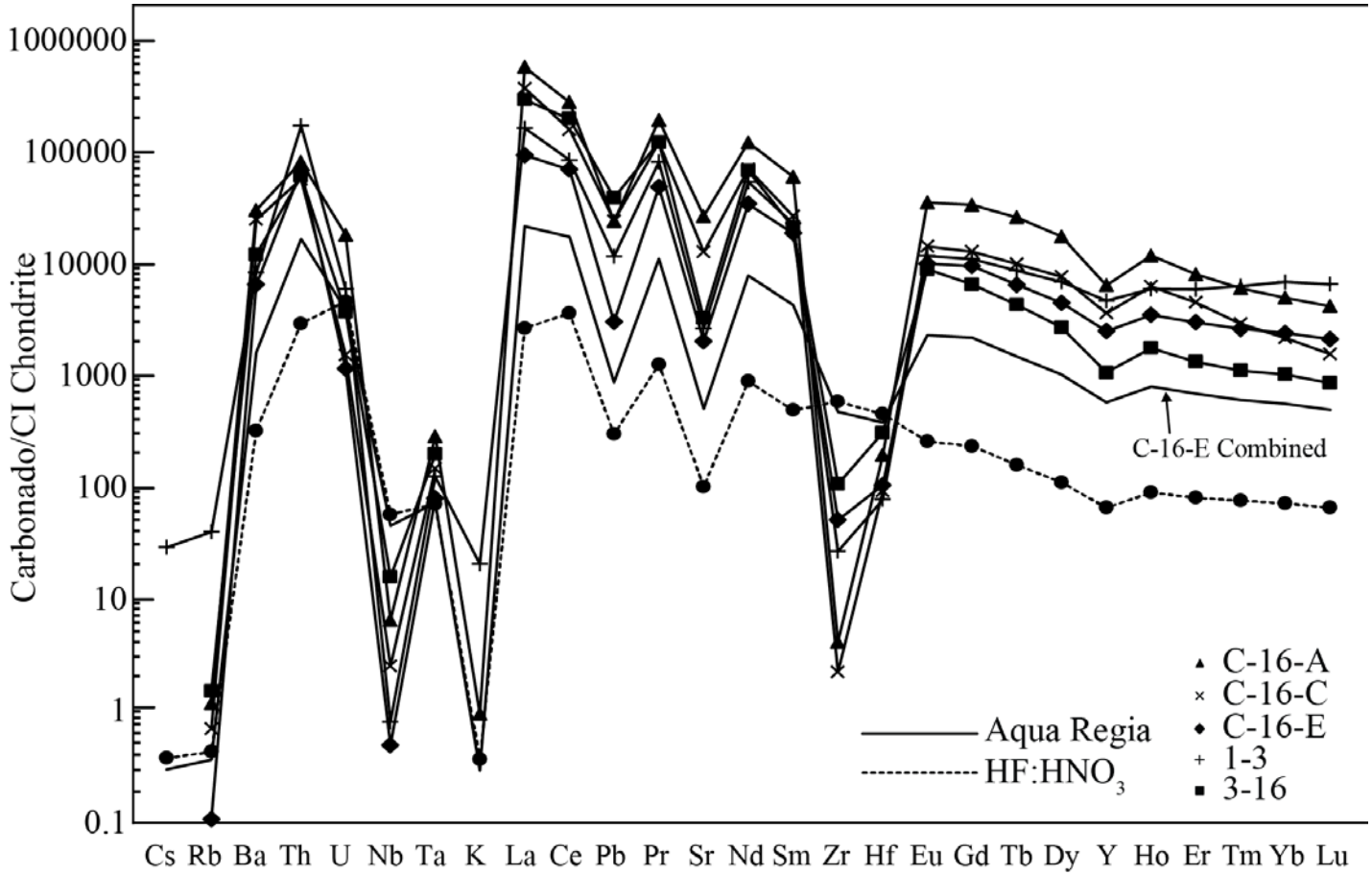

CI chondrite (McDonough and Sun 1995) normalized trace element patterns of all aqua regia and HF:HNO_3 leachates.

3.4 DISCUSSION

Sample C-16-E (combined) trace element data are likely the most representative of a whole-rock composition as they provide a concentration of all the removed material, after the HCl removed surface contaminants. The high concentrations of incompatible elements in the aqua regia leachates (9.6 to 42 wt. %) likely follows preferred dissolution of florencite, a REE-rich mineral that can hold 10's of wt. % REEs. Combined leachate REE concentrations for sample C-16-E are lower (2.3 wt. %), but certainly not insignificant.

Bulk-rock REE concentrations similar to C-16-E (combined) are mostly restricted to kimberlites, carbonatites, and high density fluid (HDF) inclusions in monocrystalline and fibrous diamonds (Henderson, 1984; Rege et al., 2010; Weiss et al., 2011; Zedgenizov et al., 2009). The exact origin of these melts/fluids is debated and they might even represent a petrogenetic continuum (Dalton and Presnall, 1998), nonetheless they are thought to play a crucial role in diamond genesis and mobilizing incompatible elements. Carbonatites are the most REE-enriched and are thought to arise from fractional crystallization of carbonated nephelinite, immiscibility of a carbonate-silicic melt, or low-degrees (< 1 %) of partial melting of carbonated mantle (peridotite or eclogite) (Jones et al., 2013). Kimberlites are thought to arise from similar scenarios, but with hydrous rather than carbonated components (Henderson, 1984). Furthermore carbonado's chondrite-normalized REE patterns are nearly indistinguishable, but at different concentrations, from these melts/fluids (Figure 3.5). Nearly linear patterns with high LREE/HREE and small to absent Eu and Ce anomalies are consistent with a mantle origin.

Ketcham and Koeberl (2013) argue in the spirit of parsimony that the REE-enrichment in carbonado is likely linked to its formation; the mechanism for carbonado formation is evidently rare and to be followed by a similarly rare incompatible-element

enrichment event seems improbable. Thus, the most likely scenario is that the formation of carbonado is genetically linked to these melts that are also unusually enriched in REEs and thought to play a role in diamond formation.

Relative depletions in other incompatible elements further corroborate this argument. The present-day macro-inclusion suite identified in earlier studies (Trueb and De Wys, 1969, 1971; Heaney et al, 2005) evidently did not equilibrate at P-T conditions necessary for diamond synthesis and has likely been subjected to some degree of alteration by fluids infiltrating carbonado's variably permeable pore network. While the REEs are relatively chemically unreactive, they are expected to chemically behave as a cohesive package. However, it is likely that other elements, especially those that are more soluble in fluids, have been mobilized and their concentrations' altered.

Disseminated higher attenuating phases within these composites are interpreted to be predominantly florencite, which commonly forms from hydrothermal alteration of monazite. Monazite can also host high concentrations of uranium and thorium, as well as REE's. The presence of excess fissiogenic isotopes within the diamond material can be explained by recoil implantation from the radioactive decay of U-rich-inclusions and/or pore fluids. Surrounding pore-filling material with more than a few hundred ppm of uranium in close proximity (~ 10 μm) is required to produce the amount of implanted isotopes measured by Ozima et al. (1991). However, the material removed from C-16-A only has 139 ppm U and is significantly higher than the other samples. Two-endmember scenarios can be posed to explain the presence of excess fissiogenic isotopes compared to the amount of Uranium in the pore-filling material: either the excess fissiogenic isotopes may have not been implanted and must have been present during carbonado formation and included into the diamond material initially; or they were implanted and Uranium has

subsequently been lost from the pore network. The latter scenario seems more likely based on observations of the inclusion suite in the filled variety.

Uranium loss also explains the high Th/U values; U^{6+} is soluble in aqueous fluids, while Th^{4+}, the only valence state of Th, is not soluble. Thus, uranium, and other soluble elements (K and LILE's), were likely mobilized during interaction with infiltrating fluids while carbonado was residing in the crust. Oxidation of uranium would not have occurred until after the GOE at ~2.3 Ga, providing a minimum of 0.3 to 1.5 Ga (based on the minimum and maximum age estimates of carbonado) for fissiogenic isotopes from the decay of uranium to be implanted into the diamond material.

Despite carbonado's likely interaction with infiltrating secondary fluids, there are still strong similarities between the geochemical behavior of carbonatite and carbonado. Negative anomalies in Cs, Rb, and K when compared to CI chondrite are common in carbonatites and present in our data. Concentrations of HFSEs, which are insoluble in aqueous fluids, in carbonado pore-filling material may have likely remained relatively unchanged. Large negative Zr and Hf anomalies are a significant feature of most carbonatites (Nelson et al., 1988), which are prominent features in all of our aqua regia leachates and C-16-E (combined). These depletions are not apparent in the HF:HNO_3 leachate, but may be caused by partial dissolution of detrital zircon, which has been identified on the surface of at least two samples (see Figure 3.1, above). The reported HFSE depletions may be a result of our dissolution process, as acid leaching does not provide information on the mineralogy and extent of material being removed. However, Figure 2.15 illustrates that a rind of material was completely dissolved in C-16-C and almost completely dissolved in 1-3, except sparse highly-attenuating phases. Thus, the C-16-E combined value, which represents all of the removed material after HCl dissolved surface contaminants, is likely reflective of the actual concentrations. We also calculated the

combined concentration from all 3 leachates, but this insignificantly changes the REE patterns or concentrations. Nb and Ta concentrations in carbonatites are variable but depletions in these elements as well as Zr and Hf are thought to arise from the presence of rutile and zircon, respectively. The measured HFSE depletion in carbonado suggests they formed from a source with residual rutile and zircon, which are common phases in eclogite and very rarely found in non-metasomatized peridotite (Kalfoun et al., 2002). We hypothesize that the geochemistry of the carbonado inclusion suite is most consistent with carbonado forming in association with carbonatite melts, from small-scale carbon-supersaturated, incompatible-element-rich fluids evolved from low degree partial melting of carbonated eclogite.

Figure 3.5 REE Diagram Comparing Carbonado to Carbonatite and Kimberlite

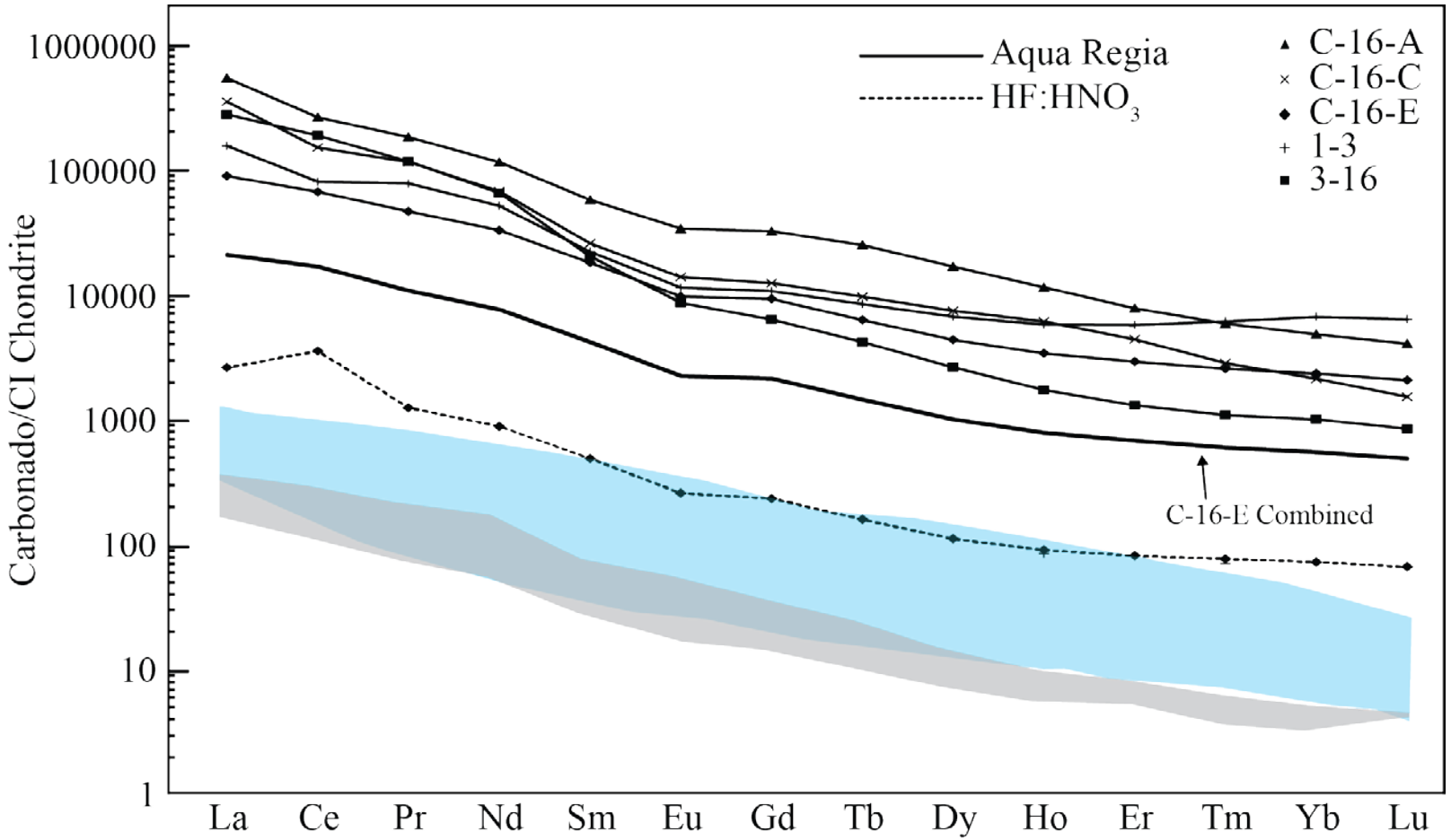

CI chondrite (McDonough and Sun, 1995) normalized REE patterns for carbonado compared to carbonatite (blue) (Jones et al., 2013; Nelson et al., 1988) and kimberlite (gray) (kimberlite standards MY-4 and SARM-39)

Chapter 4: Conclusions

4.1 Introduction

The main conclusions of this study are:

1. The internal textures in carbonado are complex and variable in detail, and no single texture of pore-filling material can be considered characteristic. We have identified new classifications for carbonado forming a continuum based on the extent of non-diamond material filling pores.
2. We document a common pore fabric that is endemic to almost all carbonado. They form a foliation with a mild preferred orientation and have similarly bladed shapes. This texture can arise from simple shear deformation.
3. The leachable material in carbonado's pore network is highly enriched in incompatible elements. The REE concentration in the "bulk" carbonado is 2.3 wt. % and has a nearly linear pattern with a LREE enrichment when normalized to chondrite. Similar bulk-rock REE patterns and concentrations are restricted to carbonatites and kimberlites, which are thought to play an important role in diamond formation. Furthermore, the measured HFSE depletion in carbonado is similar to carbonatite that formed from partial melting of carbonated eclogite that had residual rutile and zircon.

4.2 Augmented model for carbonado genesis

Taking all evidence together, we build upon the model outlined by Ketcham and Koeberl (2013) proposing that carbonado formed in a carbon-supersaturated, incompatible-element-rich fluid. We augment this model by providing a geochemical link to the origin of this fluid. The measured REE patterns and HFSE depletions are consistent with low

degree partial melting of carbonated eclogite. This proto-carbonado mass was a loosely aggregated slurry of fluids and solids carbon-saturation as the driving force for diamond crystallization. The 10-250 μm diamond "phenocrysts" would have grown during this first stage of diamond growth. Initially, the carbon-bearing media was in equilibrium with some non-diamond phases and may have reacted with others, evidenced by remnant shapes of both pristine and resorbed primary crystalline phases. This initial crystallization event would have undergone relatively high nucleation rates to create the larger, euhedral mode of diamond "phenocrysts" and as carbon was consumed, reentrant growth features formed.

The lack of dissolution features in the state-1 diamonds, however, indicates that carbon consumption was incomplete. Simple shearing of the loosely aggregated proto-carbonado mass, likely in association with ultra-reduced H_2-CH_4 fluids, induced a preferred orientation of fluid-filled pores. The ultra-reduced inclusion suite in the microdiamond groundmass, requires that the drop in oxygen fugacity was coeval with deformation. Such a drop in oxygen fugacity would lead to speciation of any remaining carbon in the fluids and redox freezing, causing a near instantaneous increase in diamond nucleation and crystallization rates. Once crystallization of the entire carbonado mass was finished, deformation was completed, based on the preservation of separate non-diamond phases (the euhedral pseudomorphs identified in this study and by Ketcham and Koeberl (2013)) that were undeformed; hence, requiring deformation to occur coevally with, or shortly before redox freezing.

The final polycrystalline diamond retained the frozen deformed fabric, hosting fluids and minerals in the non-diamond interconnected matrix. The lack of aggregated nitrogen in the microdiamond groundmass requires that entrainment and ascent to the crust occurred shortly after final crystallization. Any annealing could only have occurred when

carbonado was still at thermodynamically favorable P-T conditions to allow for atoms to migrate in the diamond crystal lattice (*i.e.* mantle conditions). Decompression of the trapped fluids during ascent to the surface, led to devolatilization and gas escape, leaving residual incompatible-element-rich mineral phases. Obviously the present-day mineral assemblage did not form at diamond-forming depths, but are instead the alteration products of the aforementioned incompatible-element-rich phases that were left behind after devolatilization. Subsequent alteration of pore-filling minerals occurred in association with infiltration of fluids through permeable regions of non-annealed microcrystalline carbonado matrix. The resulting pore-filling material likely retains characteristics of the primary mineralogy (*e.g*. incompatible elements), but may also have exchanged elements with the fluid (*e.g*., Th/U). In the context of our model, the highly-attenuating phases in the unfilled variety may be primary minerals that were isolated from fluid infiltration. Future analysis of these primary phases may shed further light on carbonado genesis.

4.3 CARBONADO FORMATION IN THE CONTEXT OF THE ARCHEAN MANTLE

While this model remains incomplete (*i.e.* origin of patinaed surface, nature of ultra-reduced fluid, among others), it explains most of the unusual features of carbonado except the origin of isotopically light carbon. The only known source of such light carbon in the mantle at diamond forming depths is recycling of organic material. We postulate that carbonado formed in associations with carbonated eclogite, the carbon isotopic signature of which was substantially derived from organic matter and organic carbon cycling processes. Subduction is the likely mechanism for introducing crustal material to diamond-forming depths during carbonado formation at 2.6 to 3.8 Ga.

Appendix A: Blob3D and Quant3D Grayscale Thresholds

Sample	Blob3D	Quant3D
C-16-A*	27-255	6500-65535
C-16-B*	32-255	7088-65535
C-16-C	9000-65535	10013-65535
C-16-D	0-2000	0-1900
C-16-E	5000-65535	4959-65535
K+K	7800-65535	-
1-3	4250-65535	5154-65535
2-11	0-2600	0-2000
3-15	6500-65535	6500-65535
Framesite	0-1400	-
1-6	-	6400-65535
3-18	-	0-2300
M8348	-	11000-65535
N628	-	0-6000

* Analyzed using 8-bit data

References

Brenker, F. E., Vincze, L., and Szymanski, A., 2008, Detection of a REE-rich, F-, and P-bearing fluid component in superdeep diamonds from Kankan (Guinea): Extended abstracts of 9th Int. Kimberlite Conf., Frankfurt, Germany, v. 9IKC-A-00390.

Cartigny, P., 2005, Stable isotopes and the origin of diamond: Elements, v. 1, no. 2, p. 79-84.

Dalton, J. A., and Presnall, D. C., 1998, The continuum of primary carbonatitic–kimberlitic melt compositions in equilibrium with lherzolite: data from the system CaO–MgO–Al2O3–SiO2–CO2 at 6 GPa: Journal of Petrology, v. 39, no. 11-12, p. 1953-1964.

De, S., Heaney, P. J., Hargraves, R. B., Vicenzi, E. P., and Taylor, P. T., 1998, Microstructural observations of polycrystalline diamond: a contribution to the carbonado conundrum: Earth and Planetary Science Letters, v. 164, no. 3-4, p. 421-433.

De, S., Heaney, P. J., Vicenzi, E. P., and Wang, J., 2001, Chemical heterogeneity in carbonado, an enigmatic polycrystalline diamond: Earth and Planetary Science Letters, v. 185, no. 3-4, p. 315-330.

Deines, P., Harris, J., and Gurney, J., 1993, Depth-related carbon isotope and nitrogen concentration variability in the mantle below the Orapa kimberlite, Botswana, Africa: Geochimica et Cosmochimica Acta, v. 57, no. 12, p. 2781-2796.

Demény, A., Nagy, G., Bajnóczi, B., Németh, T., Garai, J., Drozd, V., and Hegner, E., 2011, Hydrogen isotope compositions in carbonado diamond: constraints on terrestrial formation: Central European Geology, v. 54, no. 1-2, p. 51-74.

Dismukes, J., Gaines, P., Witzk, H., Leta, D., Kear, B., Behal, S., and Rice, S., 1988, Demineralization and microstructure of carbonado: Materials Science and Engineering: A, v. 105, p. 555-563.

Garai, J., Haggerty, S. E., Rekhi, S., and Chance, M., 2006, Infrared absorption investigations confirm the extraterrestrial origin of carbonado diamonds: The Astrophysical Journal Letters, v. 653, no. 2, p. L153.

Graham, D. J., and Midgley, N. G., 2000, Technical Communication-Graphical Representation of Particle Shape using Triangular Diagrams: An Excel Spreadsheet Method: Earth Surface Processes and Landforms, v. 25, no. 13, p. 1473-1478.

Haggerty, S. E., 1999, A diamond trilogy: superplumes, supercontinents, and supernovae: Science, v. 285, no. 5429, p. 851-860.

-, 2014, Carbonado: Physical and chemical properties, a critical evaluation of proposed origins, and a revised genetic model: Earth-Science Reviews, v. 130, p. 49-72.

Heaney, P. J., Vicenzi, E. P., and De, S., 2005, Strange diamonds: the mysterious origins of carbonado and framesite: Elements, v. 1, no. 2, p. 85-89.

Henderson, P., 1984, Rare Earth Element Geochemistry, Elsevier Science.

Ishibashi, H., Kagi, H., Odake, S., Ohfuji, H., and Kitawaki, H., 2016, Relationships between textural and photoluminescence spectral features of carbonado (natural polycrystalline diamond) and implications for its origin: Geochemistry International, v. 54, no. 10, p. 882-889.

Ishibashi, H., Kagi, H., Sakuai, H., Ohfuji, H., and Sumino, H., 2012, Hydrous fluid as the growth media of natural polycrystalline diamond, carbonado: Implication from IR spectra and microtextural observations: American Mineralogist, v. 97, no. 8-9, p. 1366-1372.

Jacob, D., Wirth, R., Enzmann, F., Kronz, A., and Schreiber, A., 2011, Nano-inclusion suite and high resolution micro-computed-tomography of polycrystalline diamond (framesite) from Orapa, Botswana: Earth and Planetary Science Letters, v. 308, no. 3, p. 307-316.

Jones, A. P., Genge, M., and Carmody, L., 2013, Carbonate melts and carbonatites: Reviews in Mineralogy and Geochemistry, v. 75, no. 1, p. 289-322.

Kagi, H., and Fukura, S., 2008, Infrared and Raman spectroscopic observations of Central African carbonado and implications for its origin: European Journal of Mineralogy, v. 20, no. 3, p. 387-393.

Kagi, H., Sato, S., Akagi, T., and Kanda, H., 2007, Generation history of carbonado inferred from photoluminescence spectra, cathodoluminescence imaging, and carbon-isotopic composition: American Mineralogist, v. 92, no. 1, p. 217-224.

Kagi, H., Takahashi, K., Hidaka, H., and Masuda, A., 1994, Chemical properties of Central African carbonado and its genetic implications: Geochimica et Cosmochimica Acta, v. 58, no. 12, p. 2629-2638.

Kalfoun, F., Ionov, D., and Merlet, C., 2002, HFSE residence and Nb/Ta ratios in metasomatised, rutile-bearing mantle peridotites: Earth and Planetary Science Letters, v. 199, no. 1-2, p. 49-65.

Kaminsky, F. V., Wirth, R., and Morales, L., 2013, Internal texture and syngenetic inclusions in carbonado: The Canadian Mineralogist, v. 51, no. 1, p. 39-56.

Kamioka, H., Shibata, K., Kajizuka, I., and Ohta, T., 1996, Rare-earth element patterns and carbon isotopic composition of carbonados implications for their crustal origin: Geochemical Journal, v. 30, no. 3, p. 189-194.

Ketcham, R. A., 2005a, Computational methods for quantitative analysis of three-dimensional features in geological specimens: Geosphere, v. 1, no. 1, p. 32-41.

-, 2005b, Three-dimensional grain fabric measurements using high-resolution X-ray computed tomography: Journal of Structural Geology, v. 27, no. 7, p. 1217-1228.

Ketcham, R. A., and Carlson, W. D., 2001, Acquisition, optimization and interpretation of X-ray computed tomographic imagery: applications to the geosciences: Computers & Geosciences, v. 27, no. 4, p. 381-400.

Ketcham, R. A., and Koeberl, C., 2013, New textural evidence on the origin of carbonado diamond: An example of 3-D petrography using X-ray computed tomography: Geosphere, v. 9, no. 5, p. 1336-1347.

Kletetschka, G., Taylor, P. T., Wasilewski, P. J., and Hill, H. G., 2000, Magnetic properties of aggregate polycrystalline diamond: implications for carbonado history: Earth and Planetary Science Letters, v. 181, no. 3, p. 279-290.

McCall, G., 2009, The carbonado diamond conundrum: Earth-Science Reviews, v. 93, no. 3-4, p. 85-91.

McDonough, W. F., and Sun, S.-S., 1995, The composition of the Earth: Chemical geology, v. 120, no. 3-4, p. 223-253.

Nelson, D., Chivas, A., Chappell, B., and McCulloch, M., 1988, Geochemical and isotopic systematics in carbonatites and implications for the evolution of ocean-island sources: Geochimica et Cosmochimica Acta, v. 52, no. 1, p. 1-17.

Ozima, M., and Tatsumoto, M., 1997, Radiation-induced diamond crystallization: Origin of carbonados and its implications on meteorite nano-diamonds: Geochimica et Cosmochimica Acta, v. 61, no. 2, p. 369-376.

Ozima, M., Zashu, S., Tomura, K., and Matsuhisa, Y., 1991, Constraints from noble-gas contents on the origin of carbonado diamonds: Nature, v. 351, no. 6326, p. 472.

Petrovsky, V. A., Shiryaev, A. A., Lyutoev, V. P., Sukharev, A. E., and Martins, M., 2010, Morphology and defects of diamond grains in carbonado: clues to carbonado genesis: European Journal of Mineralogy, v. 22, no. 1, p. 35-47.

Piazolo, S., Kaminsky, F. V., Trimby, P., Evans, L., and Luzin, V., 2016, Carbonado revisited: Insights from neutron diffraction, high resolution orientation mapping and numerical simulations: Lithos, v. 265, p. 244-256.

Rege, S., Griffin, W. L., Pearson, N., Araújo, D., Zedgenizov, D., and O'Reilly, S. Y., 2010, Trace-element patterns of fibrous and monocrystalline diamonds: insights into mantle fluids: Lithos, v. 118, no. 3, p. 313-337.

Roeller, K., and Trepmann, C., 2010, Stereo32.

Rondeau, B., Sautter, V., and Barjon, J., 2008, New columnar texture of carbonado: Cathodoluminescence study: Diamond and Related Materials, v. 17, no. 11, p. 1897-1901.

Sano, Y., Yokochi, R., Terada, K., Chaves, M. L., and Ozima, M., 2002, Ion microprobe Pb–Pb dating of carbonado, polycrystalline diamond: Precambrian Research, v. 113, no. 1-2, p. 155-168.

Sautter, V., Lorand, J.-P., Cordier, P., Rondeau, B., Leroux, H., Ferraris, C., and Pont, S., 2011, Petrogenesis of mineral micro-inclusions in an uncommon carbonado: European Journal of Mineralogy, v. 23, no. 5, p. 721-729.

Shelkov, D., Verkhovsky, A., Milledge, H., and Pillinger, C., 1997, Carbonado: A comparison between Brazilian and Ubangui sources with other forms of microcrystalline diamond based on carbon and nitrogen isotopes: Geologiya i Geofizika, v. 38, no. 2, p. 315-322.

Shibata, K., Kamioka, H., Kaminsky, F. V., and Koptil, V. I., 1993, Rare earth element patterns of carbonado and yakutite: evidence for their crustal origin: Mineralogical Magazine, v. 57, p. 607-511.

Shirey, S. B., Cartigny, P., Frost, D. J., Keshav, S., Nestola, F., Nimis, P., Pearson, D. G., Sobolev, N. V., and Walter, M. J., 2013, Diamonds and the geology of mantle carbon: Reviews in Mineralogy and Geochemistry, v. 75, no. 1, p. 355-421.

Shirey, S. B., and Richardson, S. H., 2011, Start of the Wilson cycle at 3 Ga shown by diamonds from subcontinental mantle: Science, v. 333, no. 6041, p. 434-436.

Smith, J., and Dawson, J., 1985, Carbonado: Diamond aggregates from early impacts of crystal rocks?: Geology, v. 13, no. 5, p. 342-343.

Sobolev, V., and Sobolev, N., New evidence on subduction to great depths of the eclogitized crustal rocks, *in* Proceedings Dokl Akad Nauk1980, Volume 250, p. 683-685.

Stachel, T., Harris, J. W., and Muehlenbachs, K., 2009, Sources of carbon in inclusion bearing diamonds: Lithos, v. 112, p. 625-637.

Stern, R. J., and Miller, N. R., 2018, Did the transition to plate tectonics cause Neoproterozoic Snowball Earth?: Terra Nova, v. 30, no. 2, p. 87-94.

Trueb, L., and Butterman, W., 1969, Carbonado: A microstructural study: Am. Mineralogist, v. 54, p. 412-425.

Trueb, L., and De Wys, E., 1969, Carbonado: natural polycrystalline diamond: Science, v. 165, no. 3895, p. 799-802.

-, 1971, Carbon from Ubangi-A microstructural study: American Mineralogist, v. 56, p. 1252-1256.

Weiss, Y., Griffin, W., Bell, D., and Navon, O., 2011, High-Mg carbonatitic melts in diamonds, kimberlites and the sub-continental lithosphere: Earth and Planetary Science Letters, v. 309, no. 3, p. 337-347.

Woodcock, N., and Naylor, M. A., 1983, Randomness testing in three-dimensional orientation data: Journal of Structural Geology, v. 5, no. 5, p. 539-548.

Yokochi, R., Ohnenstetter, D., and Sano, Y., 2008, Intragrain variation in δ13C and nitrogen concentration associated with textural heterogeneities of carbonado: The Canadian Mineralogist, v. 46, no. 5, p. 1283-1296.

Zedgenizov, D., Ragozin, A., Shatsky, V., Araujo, D., Griffin, W. L., and Kagi, H., 2009, Mg and Fe-rich carbonate–silicate high-density fluids in cuboid diamonds from the Internationalnaya kimberlite pipe (Yakutia): Lithos, v. 112, p. 638-647.